

THE FLORIDA STATE UNIVERSITY

COLLEGE OF ENGINEERING

DESIGN AND CHARACTERIZATION OF MECHANICAL
MESOPUMPS

By

OMAR M AL-RIFAI

A Thesis Submitted to the
Department of Mechanical Engineering
in partial fulfillment of the
requirements for the degree of
Master of Science

Degree Awarded:
Spring Semester, 2006

The members of the Committee approve the thesis of Omar Moustafa Al-Rifai defended on November 30, 2005.

Yousef S. Haik
Professor Directing Thesis

Ching-Jen Chen
Committee Member

Chi Fu Wu
Committee Member

Approved:

Chiang Shih, Chairperson, Department of Mechanical Engineering

Ching-Jen Chen, Dean, College of Engineering

The office of Graduate Studies has verified and approved the above named committee members.

ACKNOWLEDGEMENTS

I would like to start by showing my appreciation and gratitude to Dr. Yousef Haik who gave me the opportunity to do research with him on micropumps, the byproduct of which is this thesis. I would like to thank Dr. Haik for his invaluable guidance on my thesis, his patience and support thorough out my Masters program at Florida State University. Likewise, I also thank and appreciate the help of both of my committee members Dr. C. J Chen, and Dr. Chi Fu Wu. I appreciate Dr. C. J. Chen enlightening me with his experience, enthusiasm, and scientific knowledge. I am really proud to be a part of his group, and I would also like to thank Dr. Chi Fu Wu as he was there for me when I needed his advice and guidance towards this thesis. I would also like to recognize the Department of Mechanical Engineering for providing me with the opportunity to pursue an advanced education.

Moreover, I would like to thank Dr. Owusu, and Dr. Chapman in the Industrial Engineering Department for giving me access to the FDM machine to manufacture the meso crescent pump.

Finally I would like to dedicate my thesis to my family and friends for their prayers, support, and constant encouragement in pursuing a higher level of education. Thanks mom and dad for having confidence in me. And above all, I would like to thank Almighty God, Allah, for guiding me, making my path easy, and answering my prayers.

TABLE OF CONTENTS

LIST OF FIGURES	vi
LIST OF TABLES	viii
ABSTRACT	ix
CHAPTER 1	1
INTRODUCTION	1
1.1 Overview of Micropumps	2
1.1.1 Spiral Micropump	2
1.1.2 Von Karman Micropump	4
1.1.3 Crescent Micropump	6
1.2 Study Objective	7
1.3 Scope of Study	7
CHAPTER 2	9
EXPERIMENTAL SETUP AND APPROACHES	9
2.1 Spiral Mesopump	9
2.2 Von Karman Mesopump	11
2.3 Crescent Mesopump	13
2.4 Driving Mechanisms	20
2.4.1 Magnetically Coupled Mesopumps	20
2.4.2 Mechanically Coupled Mesopumps	22
2.5 Experimental Setup	23
2.6 Simulation of Viscous Drag Mesopumps	25
2.6.1 Simulation of Spiral Mesopump	26
2.6.2 Simulation of Von Karman Mesopump	28
CHAPTER 3	31
RESULTS & DISCUSSION	31
3.1 Meso Viscous Drag pumps Results	31
3.1.1 Results of magnetically and mechanically driven meso spiral pumps	31
3.1.2 Simulated data of meso spiral pump	34

3.1.3 Results of magnetically and mechanically driven meso Von Karman pumps.	39
3.1.4 Simulated data of meso Von Karman pump	41
3.1.5 Discussion	45
3.2 Positive Displacement Pump Results.....	46
3.2.1 Results of magnetically and mechanically driven meso crescent pump.....	46
3.2.2 Discussion	52
CHAPTER 4	54
CONCLUSIONS & RECOMMENDATIONS.....	54
4.1 Conclusions.....	54
4.2 Recommendations.....	55
REFERENCES	56
BIOGRAPHICAL SKETCH	57

LIST OF FIGURES

Figure 1 : AutoCAD view of spiral pump[2].....	3
Figure 2 : Micro Von Karman pump photograph [2]	4
Figure 3 : Von Karman fluid motion [2].....	5
Figure 4: Micro crescent pump photograph [2]	6
Figure 5 : Photograph of meso spiral pump.....	9
Figure 6 : Geometrical drawing of the rotating spiral disk [3]	10
Figure 7 : Photograph of meso Von Karman pump	12
Figure 8 : Photograph of meso crescent pump.....	13
Figure 9 : Transforming the base plate to an STL file.....	14
Figure 10: Slicing step of the meso crescent base plate.....	15
Figure 11: Generating tool paths to fill the slices of base plate.....	16
Figure 12: Transforming the triangular gear to an STL file	16
Figure 13: Slicing step of the meso crescent triangular gear	17
Figure 14: Generating tool paths to fill the slices of triangular gear	17
Figure 15: Transforming the peddler to an STL file.....	18
Figure 16: Slicing step of the meso crescent peddler	18
Figure 17: Generating tool paths to fill the slices of the peddler.....	19
Figure 18: Geometrical drawing of magnetic coupler [3]	21
Figure 19 : Magnetic coupling between motor and pump	21
Figure 20: Geometrical drawing of the mechanical coupler.....	22
Figure 21: Magnetic coupling between motor and pump	23
Figure 22: Experimental set up of viscous drag pumps.....	24
Figure 23: Experimental setup of the positive displacement pump	25
Figure 24: Spiral channel outline [3]	26
Figure 25 : Von Karman pumping geometry	28
Figure 26: Characteristic plot of a magnetically driven Spiral pump.....	32
Figure 27: Characteristic plot of a mechanically driven Spiral pump	33

Figure 28: Simulated data characterization at four speeds	35
Figure 29: Spiral pump experimental, analytical, and simulated data at 400 rpm.....	36
Figure 30: Spiral pump experimental, analytical and simulated data at 600 rpm.....	37
Figure 31: Spiral pump experimental, analytical, and simulated data at 900 rpm.....	37
Figure 32: Spiral pump experimental, analytical, and simulated data at 1200 rpm.....	38
Figure 33: Characteristic plot of a magnetically driven Von Karman pump.....	39
Figure 34: Characteristic plot of a mechanically driven Von Karman pump	40
Figure 35: Simulated characterization for meso Von Karman pump	42
Figure 36: Von Karman experimental and simulated data at 400 rpm	43
Figure 37: Von Karman experimental and simulated data at 600 rpm	43
Figure 38: Von Karman experimental and simulated data at 900 rpm	44
Figure 39: Von Karman experimental and simulated data at 1200 rpm	44
Figure 40: Characteristic plot of a magnetically driven crescent pump	47
Figure 41: Characteristic plot of a mechanically driven crescent pump.....	48
Figure 42: Crescent pump experimental data at 50 rpm.....	50
Figure 43: Crescent pump experimental data at 124 rpm.....	51
Figure 44: Crescent pump experimental data at 131 rpm.....	51
Figure 45: Crescent pump experimental data at 140 rpm.....	52

LIST OF TABLES

Table 1: Geometrical values	11
Table 2: Flow rates summary for magnetically driven meso spiral pump.....	31
Table 3: Flow rates summary for mechanically driven meso spiral pump.....	32
Table 4: Flow rates summary for analytical results of meso spiral pump	34
Table 5: Summary of simulated out flow in (ml/sec) of meso spiral pump	35
Table 6: Flow rates summary for magnetically driven meso (V/K) pump.....	39
Table 7: Flow rates summary for mechanically driven meso (V/K) pump	40
Table 8: Summary of simulated out flow in (ml/sec) for Von Karman mesopump	41
Table 9: Flow rates summary for magnetically driven meso crescent pump	46
Table 10: Flow rates summary for mechanically driven meso crescent pump.....	47
Table 11: Parameters of the crescent pump analytical equation.....	48
Table 12: Summary of analytical data for the crescent mesopump	49

ABSTRACT

This study focuses on characterizing meso scaled pumps. These pumps match in design to micro mechanical pumps produced using surface micromachining technology. The objective of this study is to characterize the performance of the meso scaled pumps experimentally, analytically, and numerically in order to gain a better understanding of the functional behavior of micropumps.

Both types of actuations, magnetically and mechanically driven pumps, are considered in this thesis. In the magnetic actuation, noninvasive coupling occurs between applied magnetic field and magnetically actuated material deposited on a movable actuator on the pump. Several advantages are reported when utilizing the magnetic actuation, including a reduction in the heat conduction from the motor to the bio fluids and a reduction on the hardware, particularly when using micro systems.

A coupler was designed and manufactured to transmit the torque from the motor's shaft to the pump's shaft during mechanical coupling. The three micropumps to be characterized are the spiral pump, Von Karman pump, and crescent pump. These three micro pumps were fabricated at Sandia National Laboratory.

In this study, three meso scaled pumps are characterized. The characterization for each mesopump was performed by pumping liquid water. A numerical simulation using CFDRC computer code was also performed for two viscous drag pumps (spiral, and Von Karman), and a comparison between the numerical, and experimental results was performed. Furthermore experimental data was compared to that predicted by analytical solution for spiral and crescent mesopumps. Characterization curves for each mesopump are then produced to provide a description of each pump's performance; moreover factors affecting the pump's performance are discussed.

CHAPTER 1

INTRODUCTION

The main advantages of using micro-electro-mechanical systems (MEMS) are that they cost less to manufacture and can be fabricated in large quantities. MEMS technology exists in motion sensors and is used in devices such as airbag sensors. Currently, experiments are underway to apply MEMS for use in other disciplines, such as medicine, computer technology, and telecommunication.

The objective of this study is to scale up three micro mechanical pumps that were designed by Kilani [1] and Hendrix [2] and fabricated at Sandia National Laboratory. The scaled up models will be tested for the feasibility of utilizing magnetic actuation to drive the pump remotely. It will also furnish a better understanding of the behavior of the pumps, which can be used to optimize the performance of the micro pumps. It should be mentioned, however, that the work on micro pumps will continue in collaboration with Sandia National Laboratory.

The scaled up pumps are characterized numerically and experimentally with both magnetically and mechanically actuation mechanisms. Since an increase in temperature would negatively affect blood cells then mechanically coupled micropumps would be inadequate for biological applications, therefore a magnetically coupled system was considered and utilized in this study. The mechanical pumps used in this study are the spiral, Von Karman, and crescent pumps.

The next section provides an overview of the three mentioned pumps, along with an operation mechanism of each micropump.

1.1 Overview of Micropumps

1.1.1 Spiral Micropump

The spiral micropump is one that was designed by Kilani [1], fabricated at the Sanida National Laboratory, and modified later by Hendrix [2]. The spiral micropump utilizes the viscous drag forces to pump the fluid from the inlet through the outlet. It has a spiral protrusion inside the pumping chamber, and just above this protrusion, a disk is set which is allowed to rotate. The fluid is bounded by the top rotating plate, bottom fixed plate, and the channel walls. The operation mechanism of the pump starts when the plate spins, therefore keeping the fluid in contact with the plate. This occurs because of the resulting net tangential viscous stresses.

Figure 1 is an AutoCAD mask file of the spiral pump. This figure shows the spiral protrusion inside the pumping chamber which cannot be seen under a microscope because of the micropump's upper cover. The figure also shows the transmission gear train and the Torsional Ratcheting Actuator (TRA), which provides the rotational force necessary to drive the gear train which, in turn, interconnects the plate inside the pumping chamber.

Fluid close to the rotating disk will have the same velocity as that of the disk. Since the bottom plate has zero velocity, the closer the fluid is to the non rotating bottom, it will have a reduced velocity and will reach zero at the wall. Therefore, the flow velocity decreases from the maximum flow for the fluid in contact with the top rotating disk to the minimum flow at the bottom stationary plate. The pumping process involves the dragging of the fluid from the inlet located at the center of the pump chamber to the outlet located at the end of the narrow channel as displayed in Figure 1. The continuous rotation of the top plate results in continuous flow.

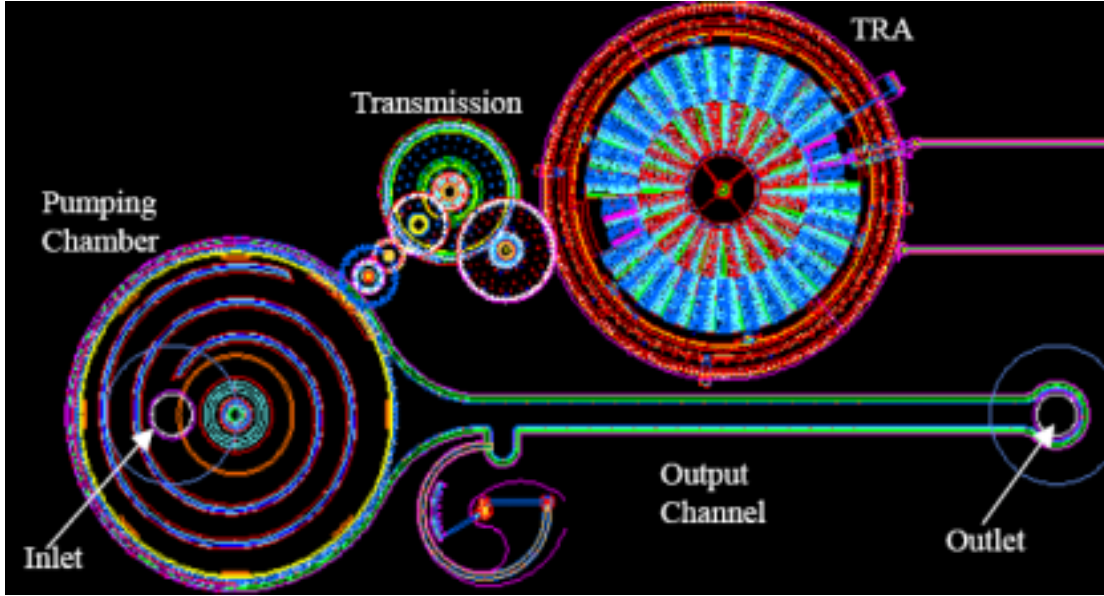


Figure 1 : AutoCAD view of spiral pump[2]

The governing equations of the generated flow were formulated based on flow and geometric conditions. Kilani [1] simplified the equations of motion. The first assumption states that the spiral channel was approximated as a straight channel. The second assumption states that symmetry of geometry and boundary conditions were noticed around the plane $Z=0$.

The final flow velocity equation is given as follows: [2].

$$u = U_{ch}(x) \frac{y}{h} - \left[\frac{h^2}{2\mu} * \frac{\Delta P}{l} + 3\delta(x) \right] \left[\frac{y}{h} - \left(\frac{y}{h} \right)^2 \right]$$

The integration of the above velocity field gives the following theoretical flow rate equation [2]

$$Q = \frac{whr}{2} * \omega - \frac{wh^3}{12\mu r(\Delta\theta)} * \Delta P$$

Where w is the wall thickness, h is channel height, r is the starting radius, ω is angular velocity, μ is the viscosity, $\Delta\theta$ is angular span, ΔP is the head pressure, and $\delta(x)$ is the derivation from the mean boundary velocity.

In this section the spiral micropump is the first viscous drag pump introduced. The next section will give a brief description of the Von Karman micropump along with its operation concept.

1.1.2 Von Karman Micropump

Von Karman pump is the second viscous drag micropump presented. This micro pump was designed by Kilani [1], and manufactured by Sandia National Laboratory. It is composed of a pumping chamber, output channel, transmission gear, and the TRA as displayed in Figure 2.

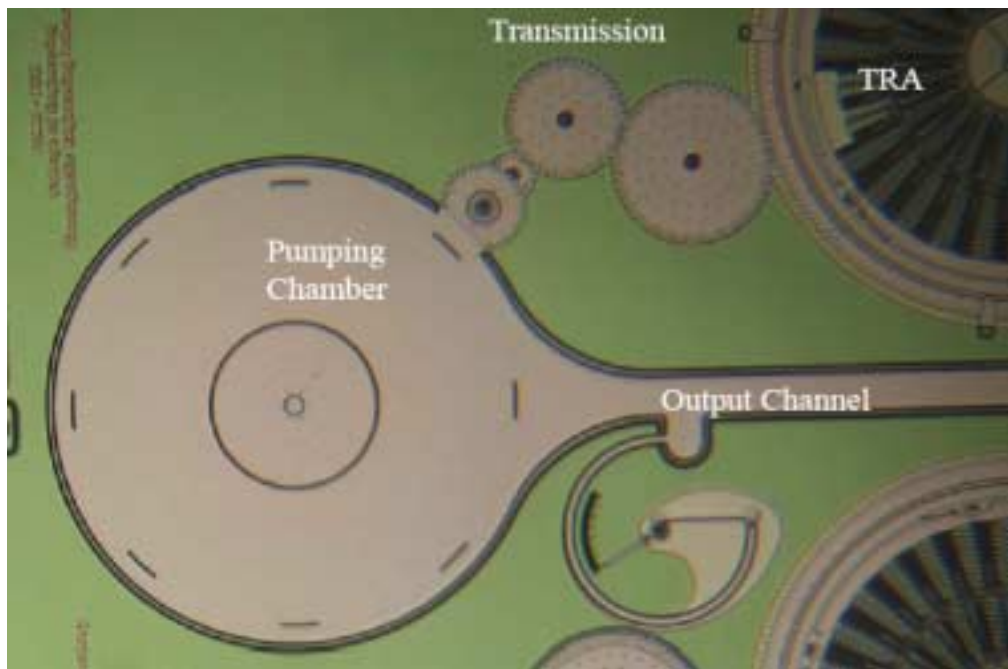


Figure 2 : Micro Von Karman pump photograph [2]

In the micro Von Karman pump when the TRA is actuated it causes the rotation of the transmission gear train. This leads to the spinning of the disk that exists inside the pumping chamber. When the disk rotates, fluid directly above the disk rotates with the disk, and due to non slip condition, the fluid is forced to move tangentially. Therefore, the fluid starts moving to replace the pumped fluid.

The described micropump was named after Von Karman because the micro pump operates on the principle of a spinning plate in a fluid. Furthermore, the micro pump's inlet is perpendicular to the spinning plate. As the classical solution suggests, the fluid will enter axially, and then is directed radially along the outlet channel. The flow motion is shown in Figure 3.

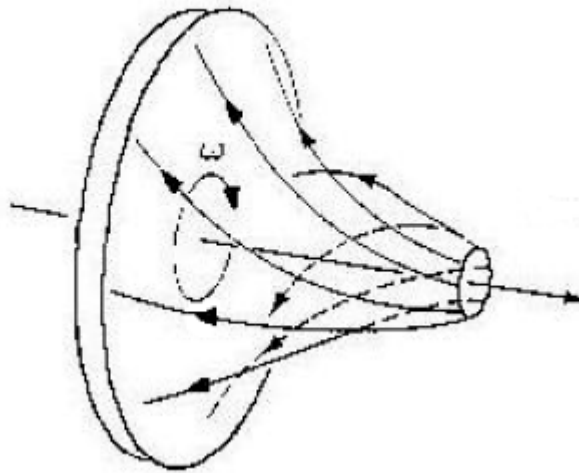


Figure 3 : Von Karman fluid motion [2]

This section introduced another viscous drag micropump, the Von Karman micro pump. An overall description of the pump's operation mechanism was discussed, which

presented the spinning flat plate concept. The next section will introduce the crescent micropump and its operation concept.

1.1.3 Crescent Micropump

The name of the crescent micropump is due to the existence of a crescent inside the pump. In addition to the crescent, the micropump includes other parts like the paddle wheel gear, and the triangular gear as show in Figure 4. This pump was designed by Kilani [1], and manufactured by Sandia National Laboratory.

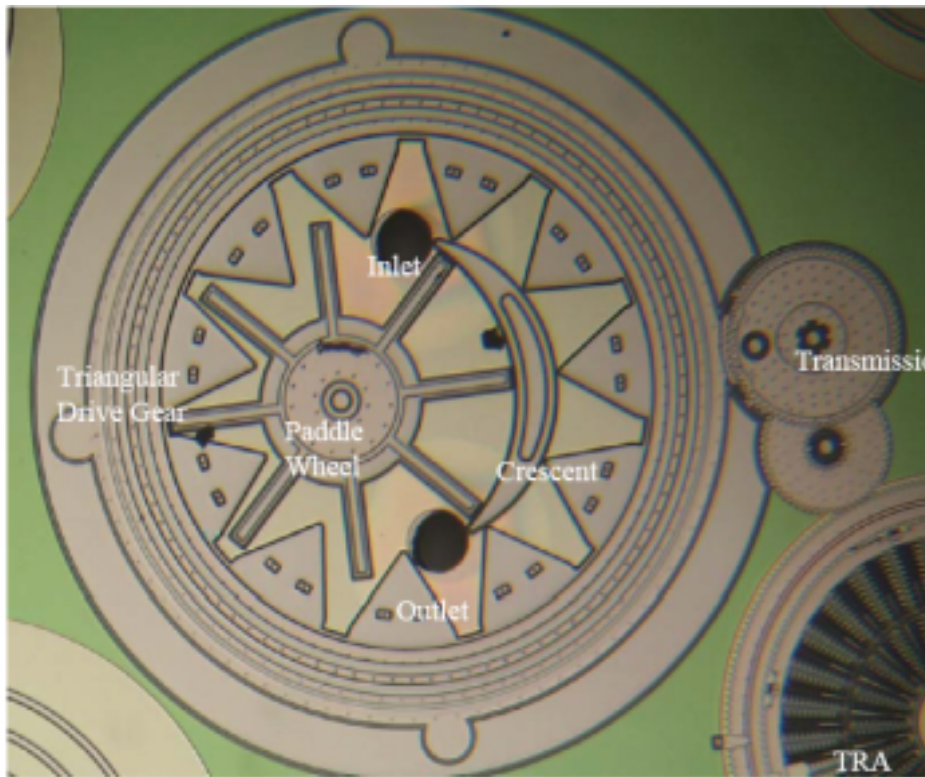


Figure 4: Micro crescent pump photograph [2]

In the micro crescent pump as the TRA is actuated, it rotates the transmission gear, which is meshed to the micro pump outer gear, causing rotation of the outer gear. When the

outer gear rotates, the triangular gear rotates, thereby actuating the peddle gear to rotate, whose teeth are meshed with the inner teeth of the ring gear. The crescent remains fixed during pumping operation because it supports the peddle gear that vibrates during rotation; moreover, it helps to trap the volume of fluid during the pumping mechanism. The peddle gear is located between the crescent and the inner teeth of the triangular gear; therefore, it is set off center from the center of the ring gear, as shown in Figure 4.

When the peddle gear rotates, the peddle arm drives the fluid from the inlet port, and as the volume of fluid approaches the outlet, the teeth of the triangular gear tries to engage again trying to make a dead space between the peddle teeth. This forces the fluid to go to nowhere but the outlet port.

This section presented the crescent micropump, and also provided an illustration of how each mechanical part of this micropump contributed to generate the final flow.

1.2 Study Objective

The interest of this study focuses on the characterization of three meso pumps. These pumps are scaled up models of already designed three micro pumps. The purpose of this study is to gain a better understanding of the micro pump's performance when it is scaled up. The research focused on the following objectives.

- A-** To design and manufacture three meso scaled pumps.
- B-** To experimentally characterize the manufactured pumps.
- C-** To computationally simulate and characterize the above two viscous drag pumps.
- D-** To analytically quantize the performance of the spiral mesopump.

1.3 Scope of Study

The research discussed in this thesis is presented in the subsequent format. Chapter one presents three micropumps that were fabricated at Sandia National Laboratory; each

pump conceptual behavior is described. Chapter two introduces three mesopumps which are scaled up models of (spiral, Von Karman, and crescent) micropumps. It also included a description of the two driving mechanisms that are employed to drive the pumps. The three mesopumps are magnetically and mechanically coupled. The chapter proceeds by illustrating the experimental set up and approaches that are utilized to experimentally run the mesopumps. Chapter two also discusses the computational analysis performed for the two viscous drag mesopumps (spiral, and Von Karman). In chapter three, results from experimentation and numerical simulation are gathered, and characteristic curves are generated to analyze the performance of each mesopump. Then the thesis is concluded with chapter four, which briefly summarizes the conclusions and provides recommendations.

CHAPTER 2

EXPERIMENTAL SETUP AND APPROACHES

2.1 Spiral Mesopump

In order to gain a better understanding of the spiral micropump concept, a spiral pump model on meso scale is fabricated and then characterized. The advantage of experimentally testing meso scaled spiral pump is to enrich our experience in the prediction of the expected generated flow.

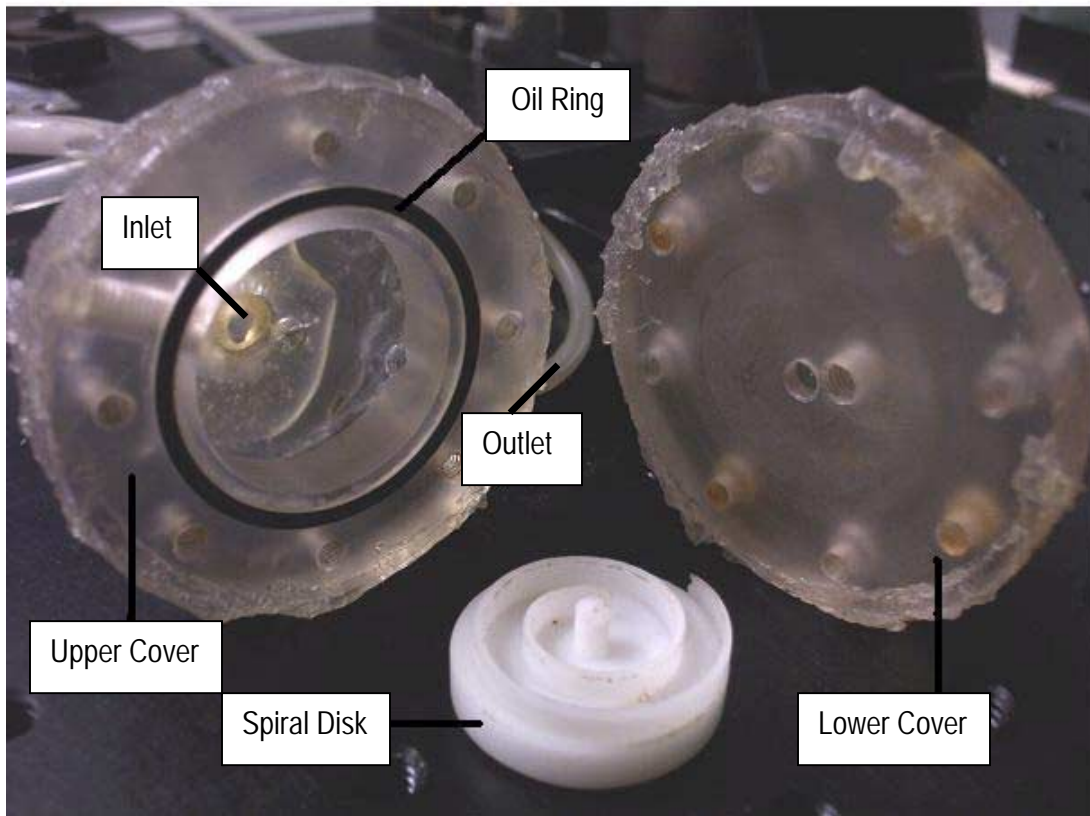


Figure 5 : Photograph of meso spiral pump

The magnetically driven meso spiral pump was designed and manufactured by Zheng [3]. The designed mesopump is composed of the upper and lower covers, spiral disk, and oil ring as shown in Figure 5. The mesopump had a leakage problem; therefore, improvements are made for this pump and silicon was used to fill up the gaps between the upper and lower covers of the pump housing. A mechanical coupler is subsequently designed and manufactured.

The spiral is set on a rotating disk and the spiral channel is machined using different radii arcs, as presented in Table 1, while the geometrical drawing of the spiral is shown in Figure 6. It is important to note that the operation mechanism of the scaled up model differs than that of the spiral micropump. In the scaled up model the mesopump is magnetically and mechanically coupled to the motor's shaft. The running motor causes the spinning of the spiral disk which drives the fluid from the inlet to the outlet tube. On the contrary, in the micro spiral pump the spiral is fixed and the plate is the one that rotates.

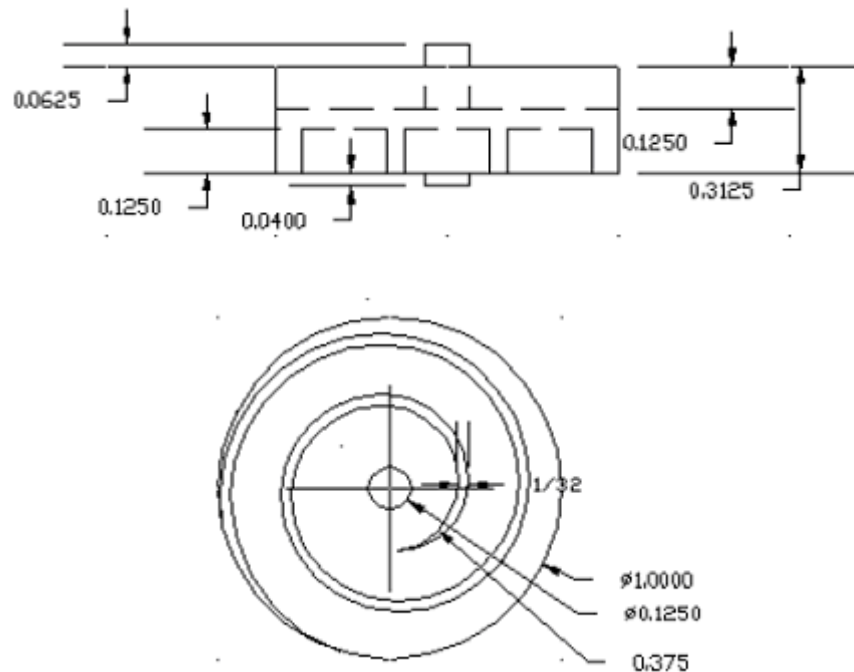


Figure 6 : Geometrical drawing of the rotating spiral disk [3]

The torque is transferred to the spiral disk without any contact. The advantage of using a magnetic coupling is that it builds up the pumping pressure and insures good sealing. A hole is drilled at the back of the spiral disk and a small cylindrical shaft is installed. A coupling is manufactured; therefore, transforming it to a mechanically driven mesopump. The two driving mechanisms are thoroughly discussed later in section 2.4.

Table 1: Geometrical values

Geometry of spiral disk	
Groove depth inch (mm)	0.125 (3.06)
Width of channel inch (mm)	0.145 (0.355)
Wall thickness w inch (mm)	1/16 (1.6)
Starting radius r inch (mm)	0.375 (9.18)
Channel height h inch (mm)	0.125(3.06)
Viscosity μ (Pa.s)	1×10^{-3}
Total angular span $\Delta\theta$	$\sim 2\pi$

This section presented the first viscous drag meso spiral pump. It also illustrated the pump's operation mechanism. The next section will introduce the Von Karman meso pump with its operation concept.

2.2 Von Karman Mesopump

Von Karman mesopump is the second viscous drag pump introduced. The idea of characterizing a meso scaled model was suggested in order to allow us to have a closer

look at the flow behavior and the pump's performance. Moreover, the characterization provides us with a prediction of the expected output flow. The mesopump is composed of the upper cover, lower cover, and rotating disk as shown in Figure 7.

The housing of the scaled up spiral pump was used and a disk was manufactured to fit in the pump housing that replaced the spiral disk. A couple of magnets were implemented at the back of the disk. In this scaled up model, the pump is driven magnetically by a magnetic coupling, therefore causing the disk to rotate. The fluid is pumped from the inlet port to the outlet port. The mechanically driven meso Von Karman pump is developed by using the same parts of the previous mesopump with small modifications applied to it.

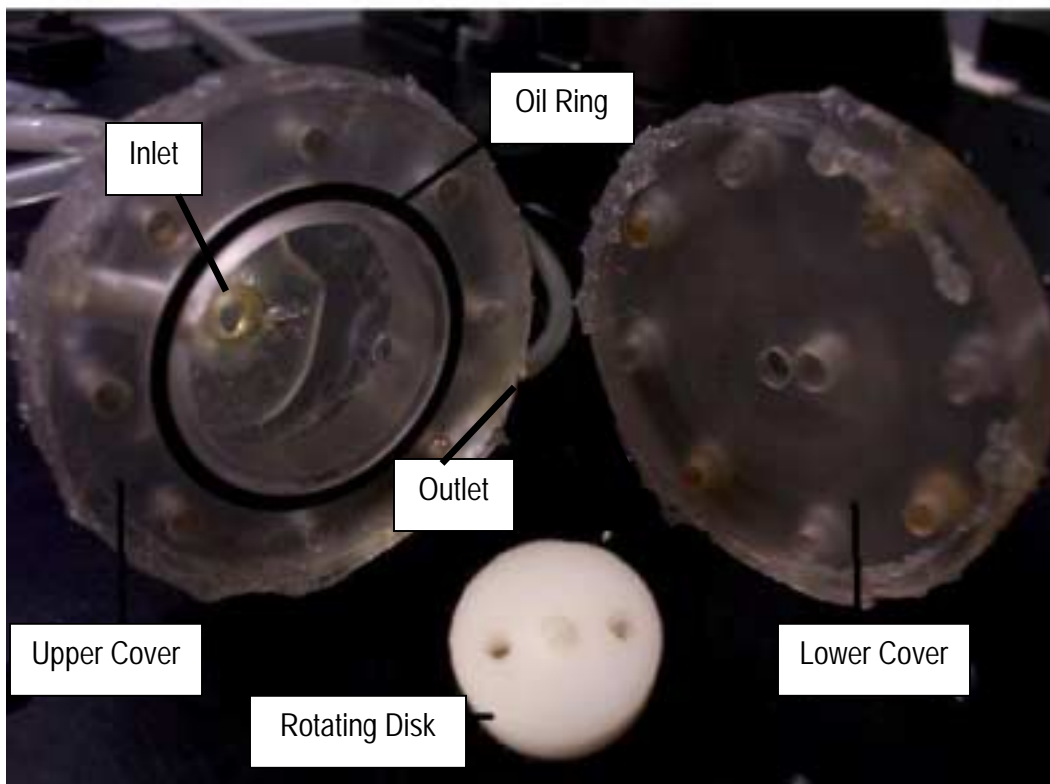


Figure 7 : Photograph of meso Von Karman pump

This section presented the Von Karman mesopump along with a thorough illustration of the pump's mechanism. The next section introduces the positive displacement pump (crescent mesopump), with a description of the pump's manufacturing process.

2.3 Crescent Mesopump

A scaled up crescent pump is designed for the purpose of performing pump characterization. Characterization is performed through experimentally testing two meso scaled crescent pumps: one is magnetically driven and the other is mechanically driven. Its importance lies in gaining better understanding of the pumping concept of the crescent pump. Figure 8 shows a photograph for the meso spiral pump that consists of the crescent, peddler, triangular gear, and an oil ring.

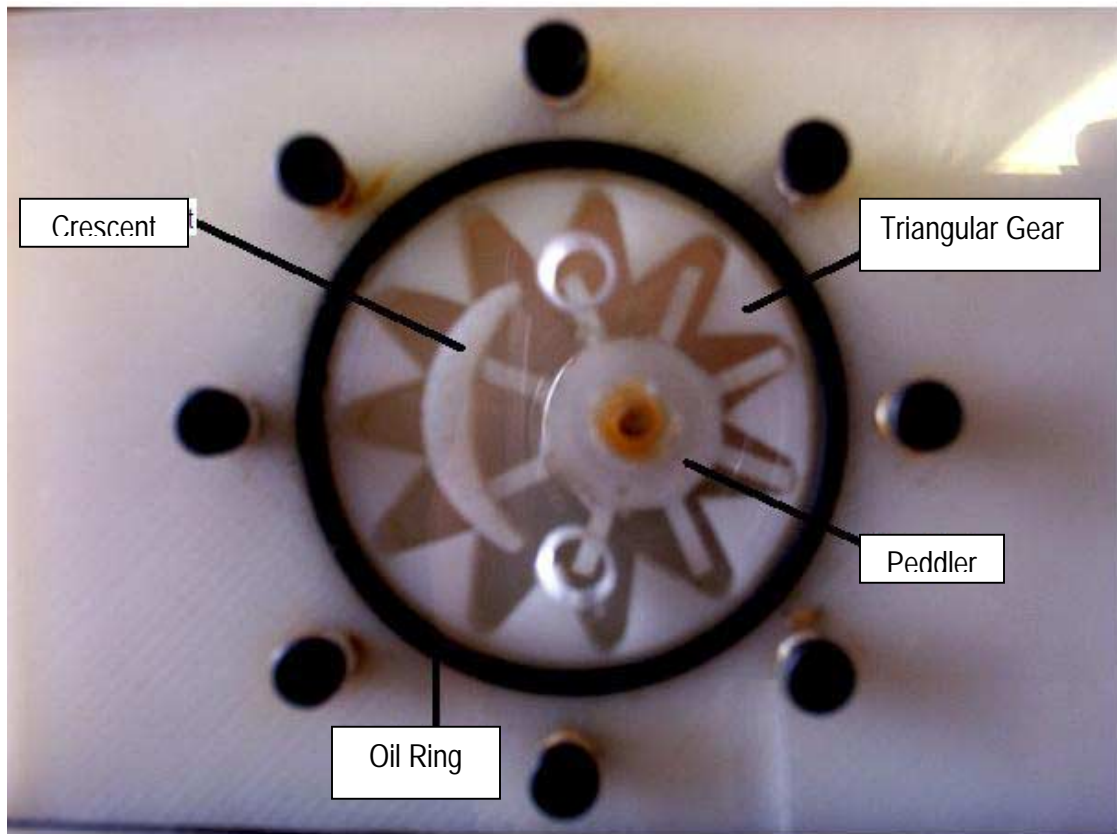


Figure 8 : Photograph of meso crescent pump

The manufacturing process of the scaled up crescent model involved several steps. First, the scaled up crescent pump is drawn on Pro/ E program and the drawings are saved as STL files. Then the Fused Deposition Modeling (FDM) machine is used to turn the CAD geometry into models that can be used for design reviews and to check if the model or the desired design can be manufactured. This machine is also called a Rapid Prototype machine. The support tip for FDM extrudes a material that supports any overhanging portions of the model's geometry. When the model is completed, the support is easily dissolved, leaving behind the final product.

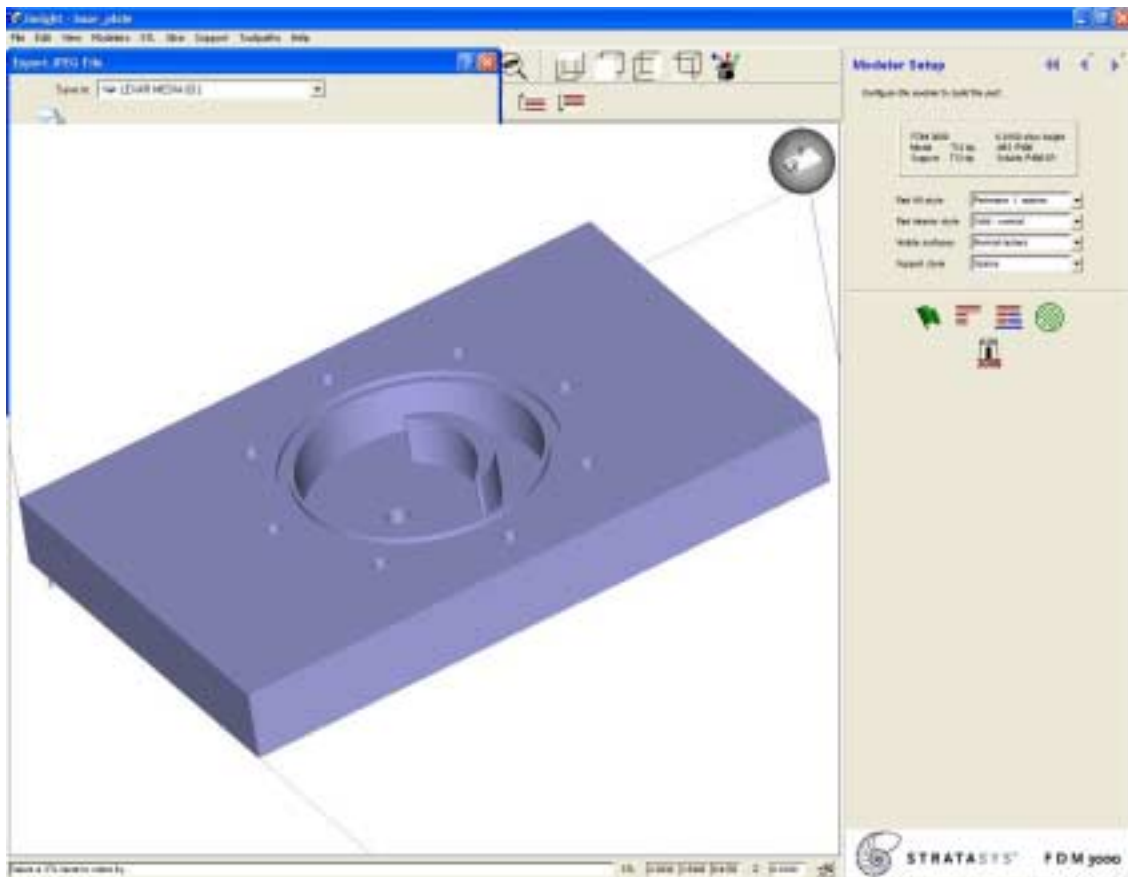


Figure 9 : Transforming the base plate to an STL file

After the model was drawn on Pro/E each part was converted to an STL format as shown in Figures 9, 12, and 15. The STL file is read into Stratasys' slicing software called *Insight*. *Insight* breaks the model into individual slices, as illustrated in Figures 10, 13, and 16 with each slice representing one layer of material. *Insight* then generates tool paths to fill the slices. This is presented in Figures 11, 14, and 17. These tool paths form the Stratasys Modeling Language (SML) file. After slicing an STL file and creating a SML file, the SML file is downloaded to FDM hardware for modeling.

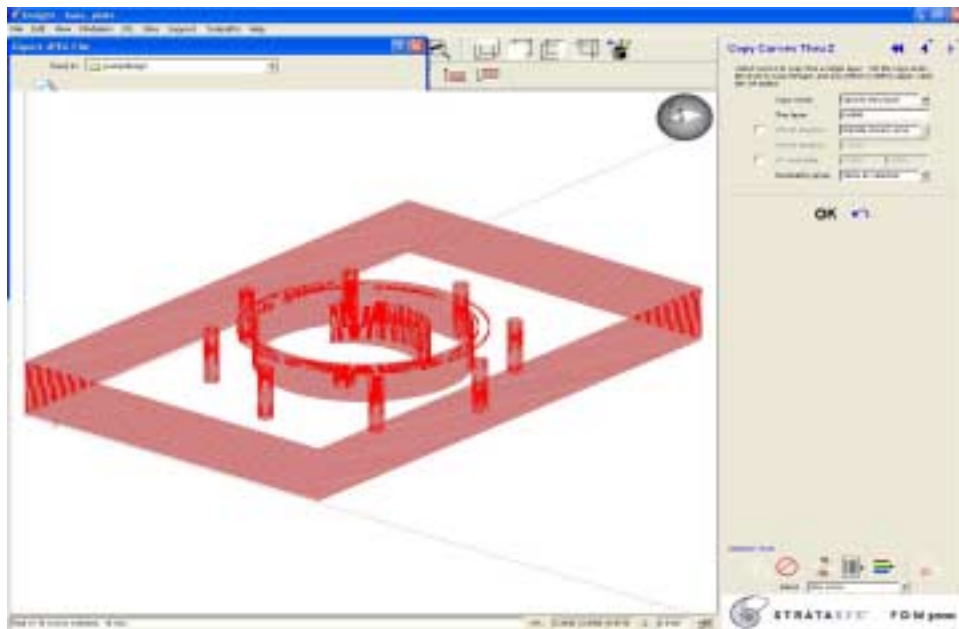


Figure 10: Slicing step of the meso crescent base plate

In the FDM hardware, the FDM head moves in two horizontal axes across a foundation and deposits a layer of material for each slice. The material is heated by the FDM head so it comes out in a semi liquid state. The successive layers fuse together and solidify to build up an accurate, three-dimensional model of the design. The model material used was 400 ABS plastic. This material is tough plastic Acrylonitrile-Styrene based material which produces hard prototypes. The 400 ABS material allows the building of models that are much more similar to the desired final product than is possible with other modeling materials.

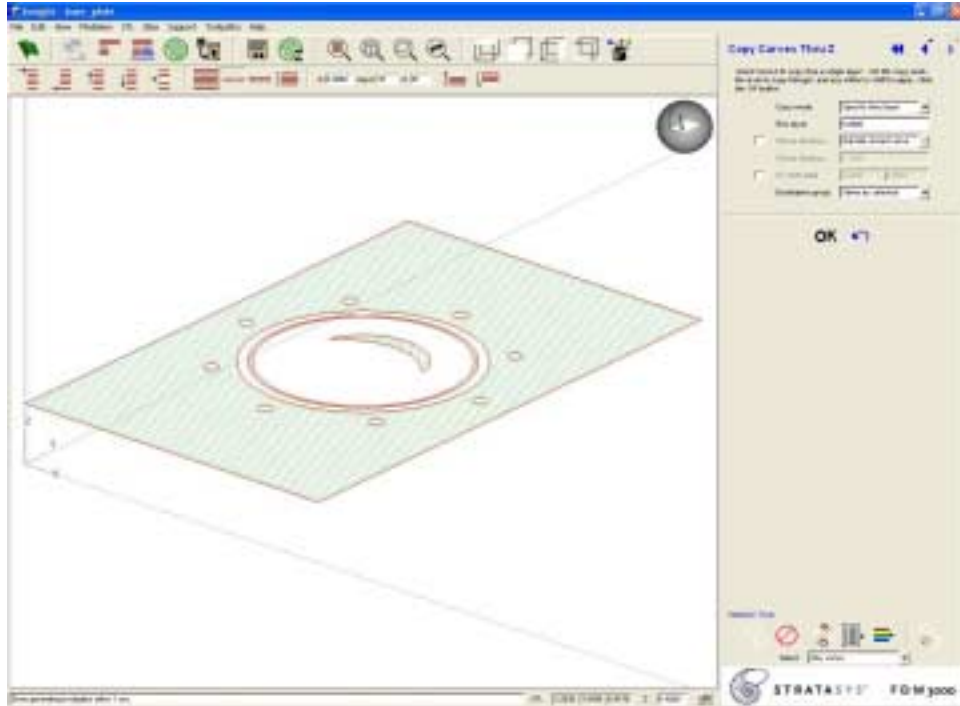


Figure 11: Generating tool paths to fill the slices of base plate

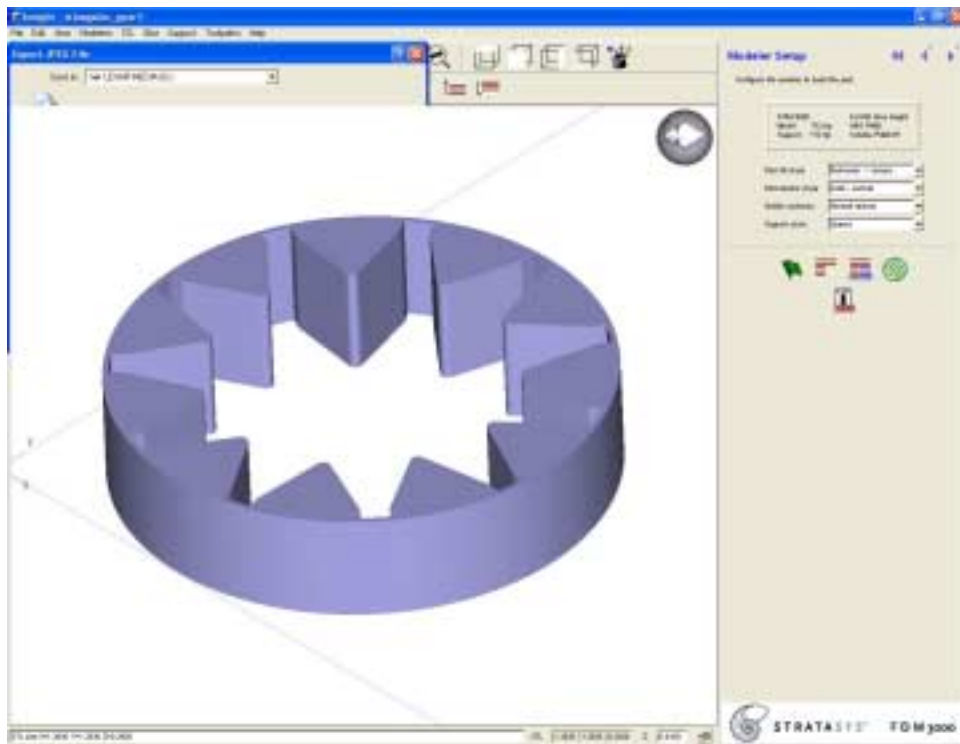


Figure 12: Transforming the triangular gear to an STL file

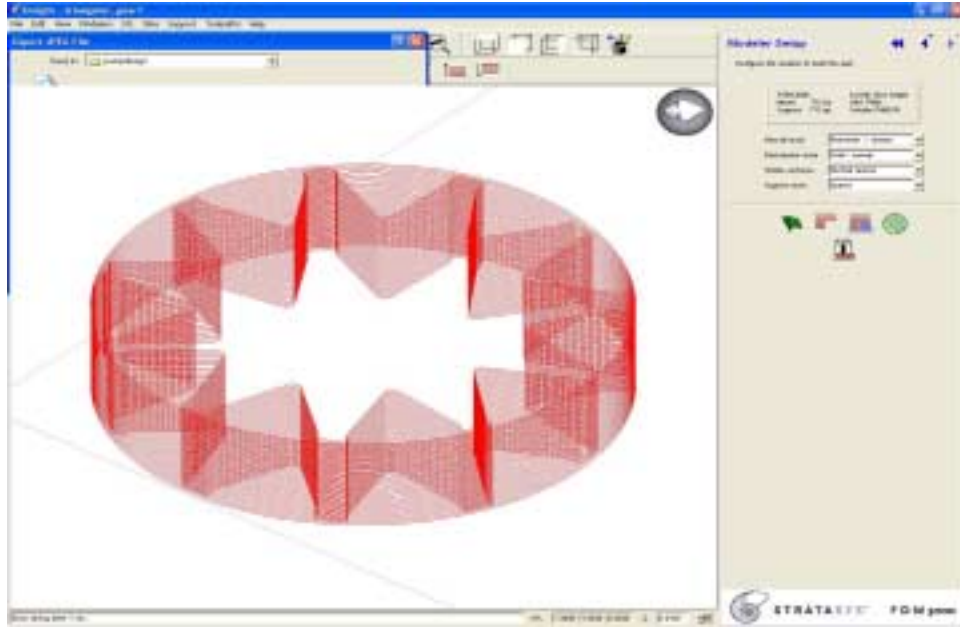


Figure 13: Slicing step of the meso crescent triangular gear

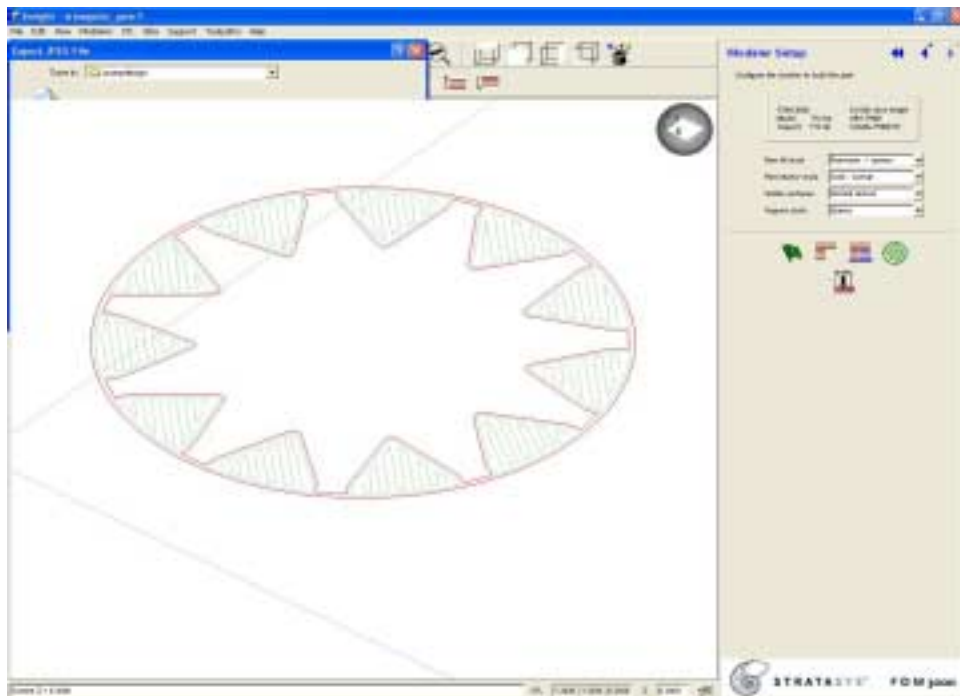


Figure 14: Generating tool paths to fill the slices of triangular gear

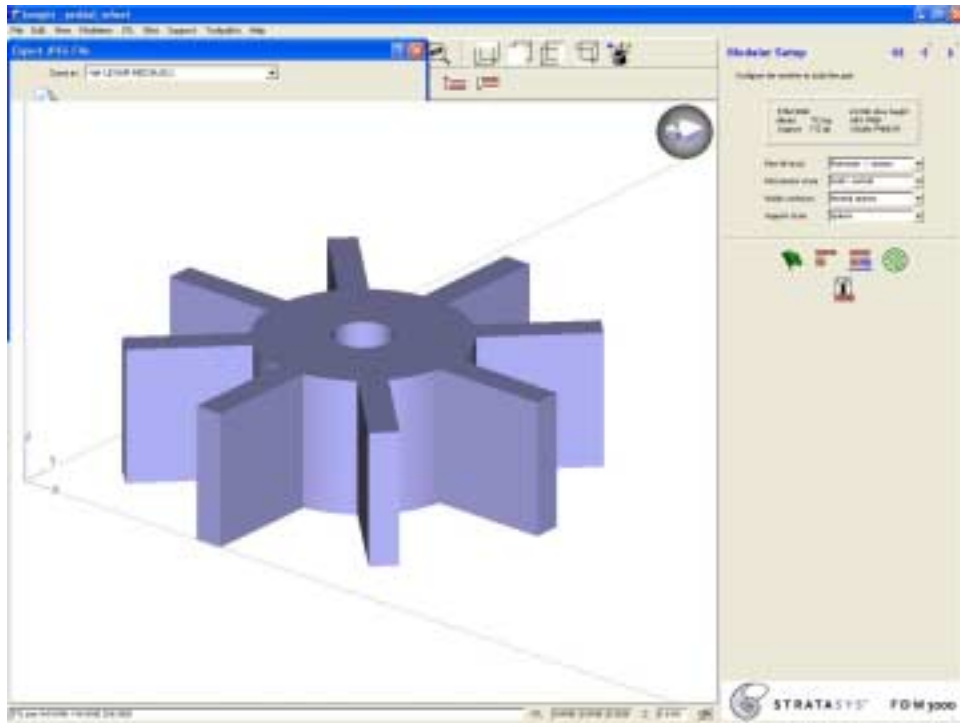


Figure 15: Transforming the peddler to an STL file

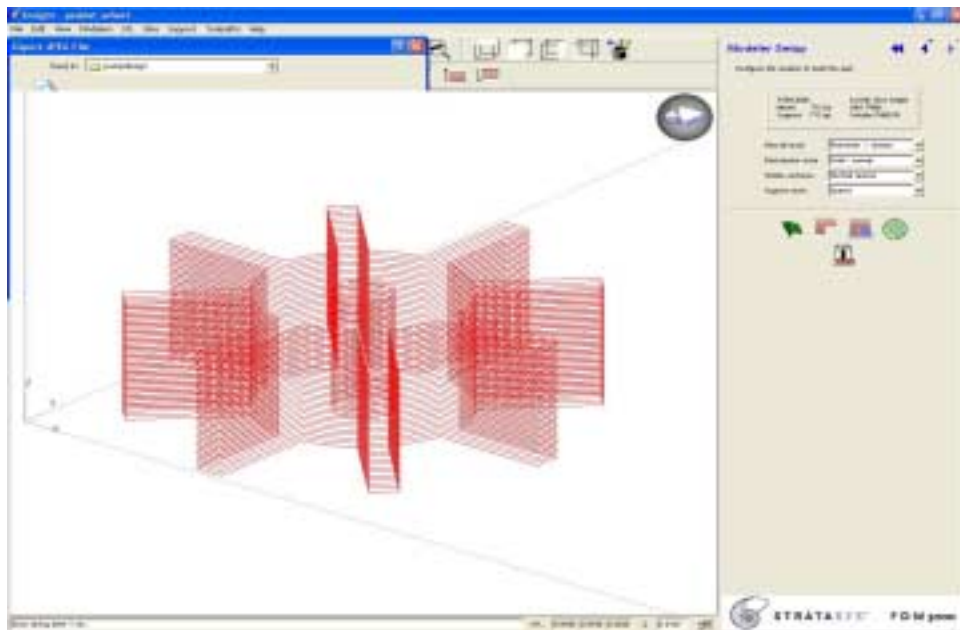


Figure 16: Slicing step of the meso crescent peddler

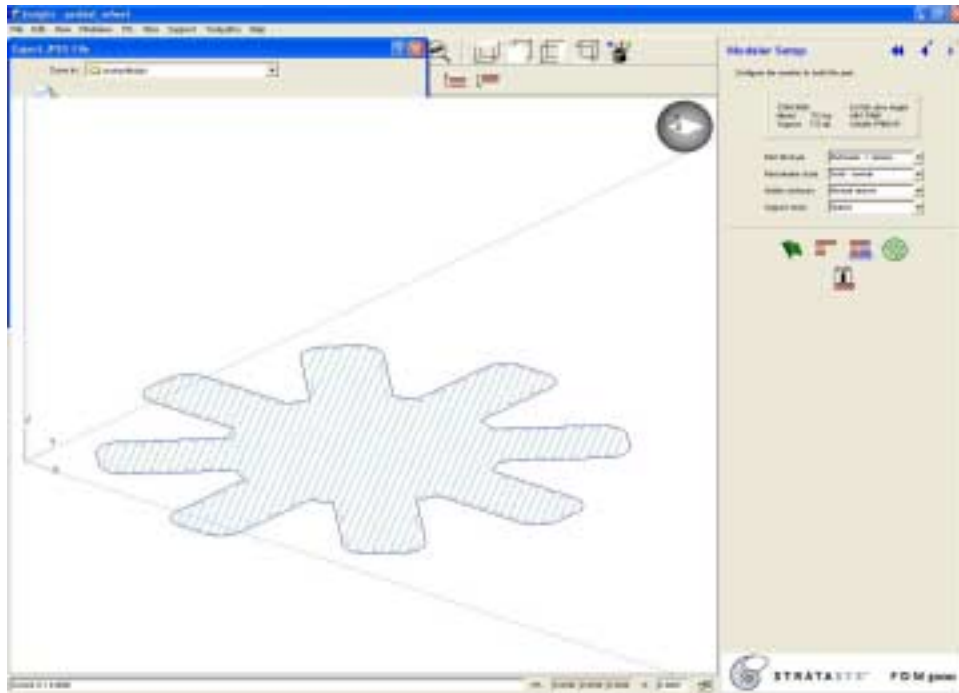


Figure 17: Generating tool paths to fill the slices of the peddler

It is important to note that the FDM machine must be set at the following temperatures: the model material must be at 270 degrees Celsius; the support material temperature at 210 degrees Celsius; and the envelop temperature at 70 degrees Celsius.

Cleaning Process:

The final process is the cleaning process, in which a clean station is used to remove the soluble support material from FDM parts, utilizing the following procedure:

- 1- Fill the tank until the water is an inch from the top of the tank (approx. 4 gallons).
- 2- Set the Temperature to 150 degrees (F).
- 3- Adding the solution concentrate (P400sc), add 1/3 of the bottle in the tank.
- 4- A small pump is used to circulate the water.

- 5- Drop the FDM parts in the tank after 3 to 5 minutes to insure that the concentrate is dissolved.

This section presented the crescent mesopump that is mechanically and magnetically driven. An illustration of the pump's operation was discussed along with the manufacturing process using the FDM machine. The next section will discuss two driving mechanisms that were utilized in order to provide the necessary torque to run the three designed mesopumps.

2.4 Driving Mechanisms

In order to run the mesopumps a motor is used, and to transport the rotational force from the motor to the pump, couplings are implemented. The three manufactured meso pumps are magnetically and mechanically driven through the use of mechanical and magnetic couplers. Each driving mechanism will be discussed and described in the next subsections.

2.4.1 Magnetically Coupled Mesopumps

The viscous drag mesopumps (spiral and Von Karman), as well as the positive displacement mesopump (crescent) are magnetically driven. This is accomplished through the use of a couple of magnets that were implemented at the back of the rotating disk, and the disk is magnetically coupled to the magnetic coupler. Figure 18 shows a schematic of the geometrical drawing of magnetic coupler which is designed and manufactured by Zheng [3].

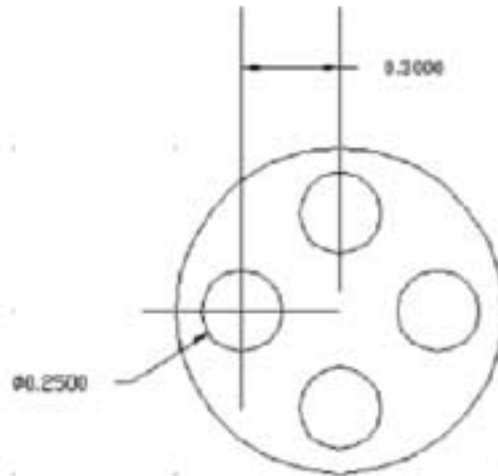


Figure 18: Geometrical drawing of magnetic coupler [3]

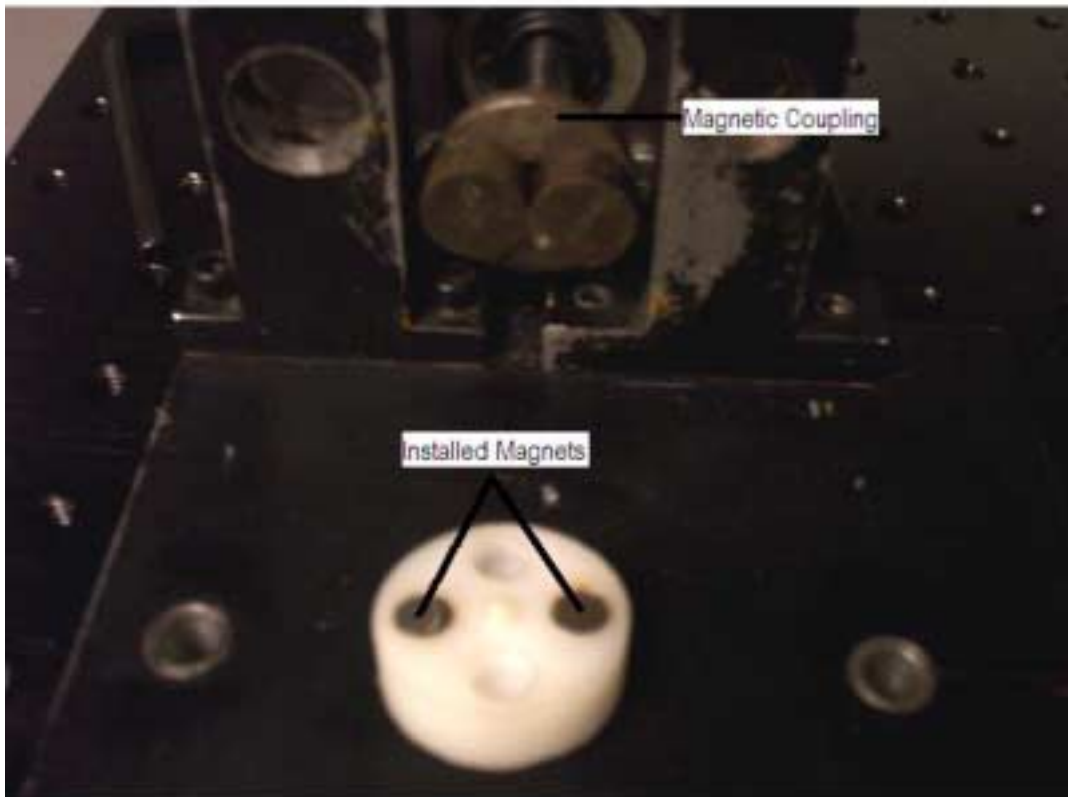


Figure 19 : Magnetic coupling between motor and pump

2.4.2 Mechanically Coupled Mesopumps

After the three mesopumps were magnetically actuated, and experimentally wet tested, some modifications were added for the three mesopumps in order to transform them to mechanically driven mesopumps. The rotating disk was drilled and a shaft was installed. Then, a mechanical coupler was used to directly connect the motor's shaft to the pump's shaft as shown in Figure 21. Following this procedure, the mesopumps were also mechanically driven.

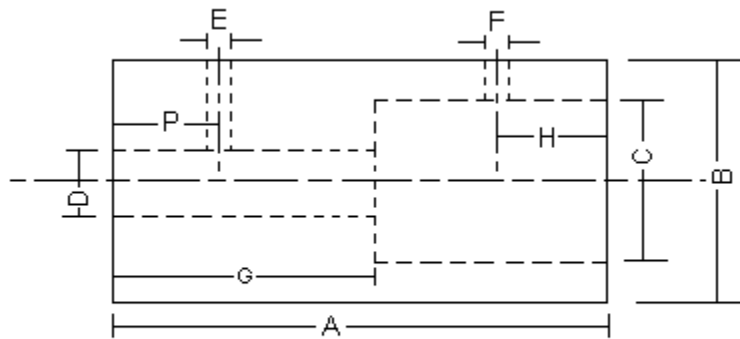


Figure 20: Geometrical drawing of the mechanical coupler

The mechanical coupler was designed and fabricated in the workshop. Figure 20 shows a sketch of the coupler with its dimensions A, B, C, D, E, F, G, H, and P. And those values are presented below in inch unit.

A= 1.023 inch	D= 0.137	G= 0.551
B= 0.551 inch	E= 0.078	H= 0.275
C= 0.314 inch	F= 0.078	P= 0.275

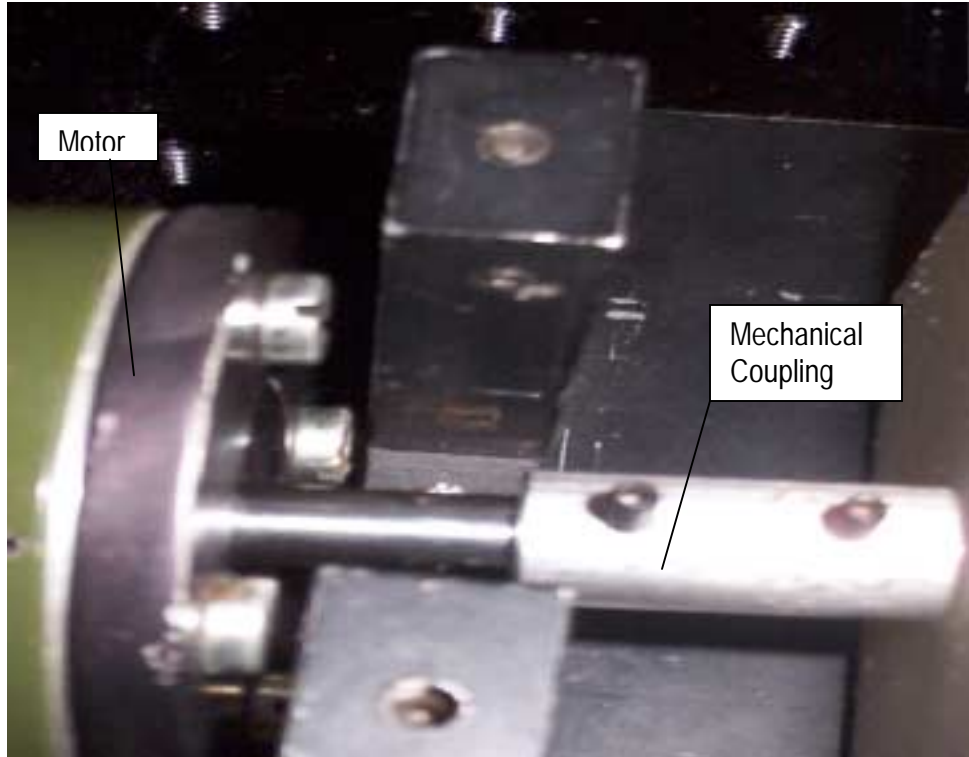


Figure 21: Magnetic coupling between motor and pump

This section described two driving mechanisms where the motive force used to generate the mechanical motion for the three mesopumps is provided by magnetic and mechanical coupling. The next section provides a thorough description of the experimental setup and the procedure followed to perform experimentation on the fabricated mesopumps.

2.5 Experimental Setup

The same experimental setup and procedure is followed for each mesopump, viscous drag pumps, and the positive displacement pump. The tools necessary to perform the experimentation are the pump, motor, reservoir tank, and power supply as presented by Figure 22 and 23. A Maxon ironless core DC motor is also used to run the mesopump models. The motor is powered up by a (0→30) volt power supply. An LCD contact

tachometer is used to measure the pump's rotational speed. The pump tests are performed at four different rotational speeds. At each speed the time needed to fill up a 10 ml volume of water at six different pressure heads is recorded. Then the data is recorded, and flow rates are calculated by dividing the volume by the time at each head.

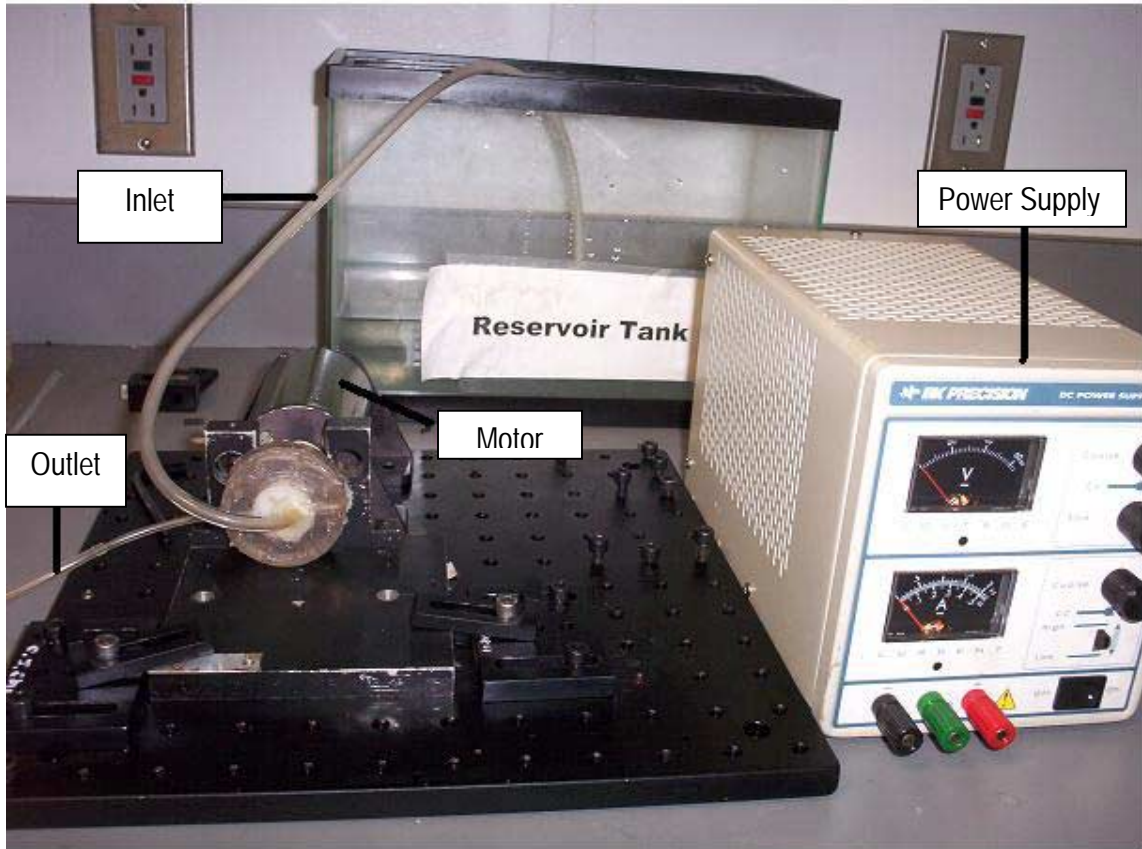


Figure 22: Experimental set up of viscous drag pumps

This section presented the experimental setup and the procedure followed to experimentally run and test two viscous drag mesopumps, and one positive displacement mesopump. The next section covers the steps taken to numerically simulate two viscous drag mesopumps (spiral, and Von Karman).

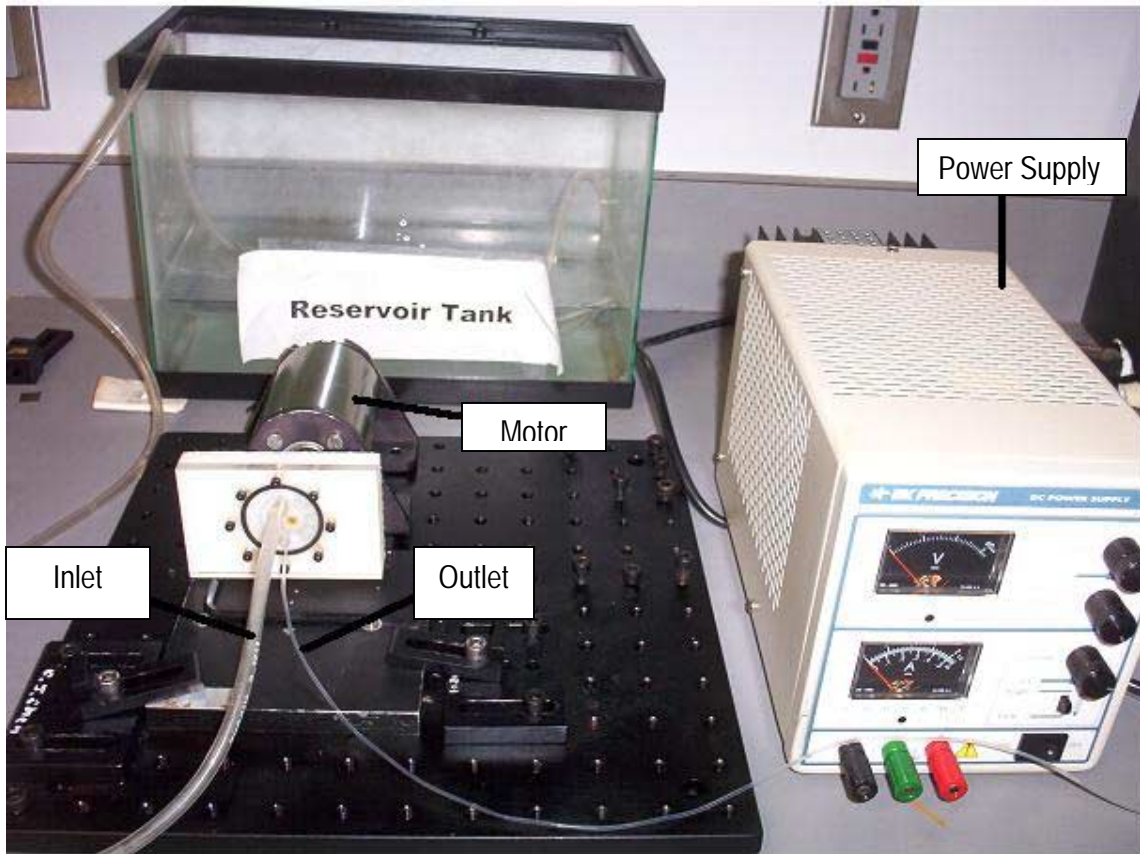


Figure 23: Experimental setup of the positive displacement pump

2.6 Simulation of Viscous Drag Mesopumps

Experimentation setup is followed by simulation using the CFDRC [4] Computational Fluid Dynamics program. Simulating the fluid flow generated by the mesopumps is important because it provides us with simulated results that can be compared to experimental results. Furthermore numerical simulation helps in shortening the time between design and fabrication of a pump which enables us to apply enhancements on the pump's design. Simulation of the meso spiral pump was performed and then followed by Von Karman mesopump simulation.

2.6.1 Simulation of Spiral Mesopump

Spiral mesopump is the first viscous drag pump that is computationally characterized. In order to perform the simulation several steps were followed. First the geometry of the flowing fluid is drawn using AutoCAD program; therefore, understanding how the flow behaves and interact is essential. For the case of the spiral mesopump the fluid will exist in the pumping chamber, and the spiral channel. The geometry is then imported to the CFDRC software.

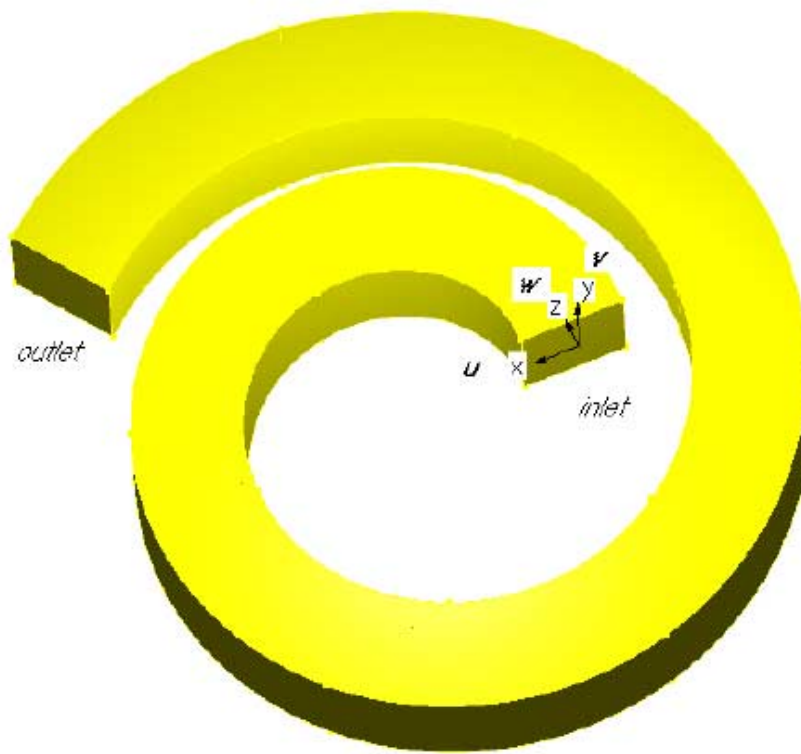


Figure 24: Spiral channel outline [3]

The next step is meshing the imported geometry of the system with linear grids. The geometry is then imported to the ACE software. The solver software allows for setting up the boundary condition. Then the software solves the equations of motion of the fluid at each grid point. The solver asks for the type of fluid used and its properties. In our case of study the fluid is liquid water with kinematic viscosity ν of $1 \times 10^{-6} \text{ m}^2/\text{sec}$, and density ρ

of 997 Kg/m³. Figure 24 shows the fluid control volume of the spiral mesopump. The stipulated boundary conditions are set where the Z inlet interface is at a total pressure P1, Z outlet is set at a fixed pressure P2. Walls at X outer, X inner, and Y Bottom are all set as rotating walls. Y top is set as a non slip wall with zero velocity.

The grid independence is tested by increasing the number of computational grids from 10,120 to 113,258 points as shown in groups (1, 2, and 3).

Group 1: Summary of 3D Grid Data

Total number of nodes: 10120

Number of quad. faces: 25170

Total Number of faces: 25170

Number of hexagon cells: 7469

Total Number of cells: 7469

Group 2: Summary of 3D Grid Data

Total number of nodes: 25341

Number of quad. faces: 71400

Total Number of faces: 71400

Number of hexagon cells: 21213

Total Number of cells: 21213

Group 3: Summary of 3D Grid Data

Total number of nodes: 113258

Number of quad. faces: 300624

Total Number of faces: 300624

Number of hexagon cells: 93741

Total Number of cells: 93741

The difference in flow rates between group one and two is less than five percent, while it is within three percent change between groups two and three in the converged solution. The convergence is set at 0.0001 change in velocity and pressure. The simulation is performed at different combinations of pressure heads and rotational speeds.

2.6.2 Simulation of Von Karman Mesopump

The second viscous drag pump that is numerically characterized is the Von Karman mesopump. The same steps were followed to perform simulation starting from geometry creation of the flow field to setting the boundary conditions.

First the pump is geometrically drawn as a three dimensional volumetric object that acts as a duplicate of the actual pump. Figure 25 shows one volume that is presented in the geometry. The pumping chamber with its internal rotating disk is labeled in the figure. Then the mesopump was divided into five regions and was labeled as shown in Figure 25. This is important in order to account for the inlet labeled as five in the figure which is located at the top of the pumping chamber. Then the five sections were joined to act as one neighboring spinning plate.

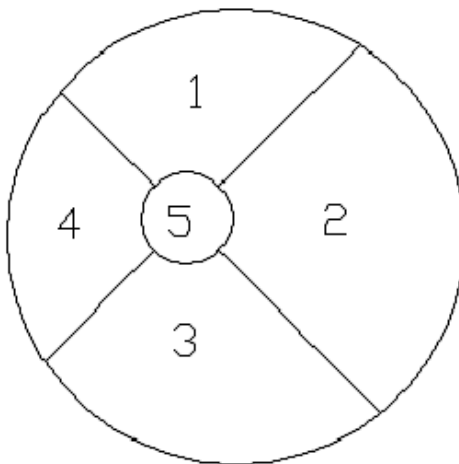


Figure 25 : Von Karman pumping geometry

The boundary conditions for the Von Karman are set by using a fixed pressure condition at the inlet and the outlet. The bottom rotating disk is set as a rotating wall, and the top of the pumping chamber is a no slip wall with zero velocity. The flow media identified in the solver is water with density ρ of 997 Kg/m³ and kinematic viscosity ν of 1×10^{-6} m²/sec.

Another test of grid dependence is also applied for the meso Von Karman pump and the 3D grid data are gathered in groups as shown below.

Group 1: Summary of 3D Grid Data

Total number of nodes: 9510

Number of quad. faces: 24560

Total Number of faces: 24560

Number of hexagon cells: 6859

Total Number of cells: 6859

Group 2: Summary of 3D Grid Data

Total number of nodes: 26470

Number of quad. faces: 72529

Total Number of faces: 72529

Number of hexagon cells: 22342

Total Number of cells: 22342

Group 3: Summary of 3D Grid Data

Total number of nodes: 112722

Number of quad. faces: 300088

Total Number of faces: 300088

Number of hexagon cells: 93205

Total Number of cells: 93205

In order to test for the grid dependence, the grid points are increased from 9,510 to 112,722 points with less than three percent change in the converged solution. The convergence condition was previously set as 0.0001 change in pressure and velocity values. The difference in flow rates between group one and two is less than five percent, while it is within three percent change between groups two and three in the converged solution. Then, simulation is performed on the scaled up model at different combinations of pressure heads and rotational speeds. The values of mass flow in g/sec are gathered, and the characteristic curves are plotted.

CHAPTER 3

RESULTS & DISCUSSION

This chapter provides results that are gathered after conducting experimentation and numerical simulation for three mesopumps. Characteristic curves for the pumps are also presented, and discussed

3.1 Meso Viscous Drag pumps Results

3.1.1 Results of magnetically and mechanically driven meso spiral pumps

The spiral mesopump is first magnetically driven and the generated flow rates results are gathered in Table 2. Then the mesopump is mechanically driven and flow rate values are summarized in Table 3. These flow rates are represented as data points in Figures 26 and 27 where the X-axis is the pressure head (P in kPa), and the Y-axis is the flow rate (Q in ml/sec).

Table 2: Flow rates summary for magnetically driven meso spiral pump

$\Delta P(\text{kPa})$	Q at 400 rpm	Q at 600 rpm	Q at 900 rpm	Q at 1200 rpm
0	0.52	0.601	0.691	0.795
0.19	0.471	0.603	0.674	0.761
0.39	0.436	0.51	0.568	0.625
0.58	0.3	0.371	0.508	0.581
0.78	0.172	0.284	0.372	0.51
0.97	0.134	0.198	0.301	0.384

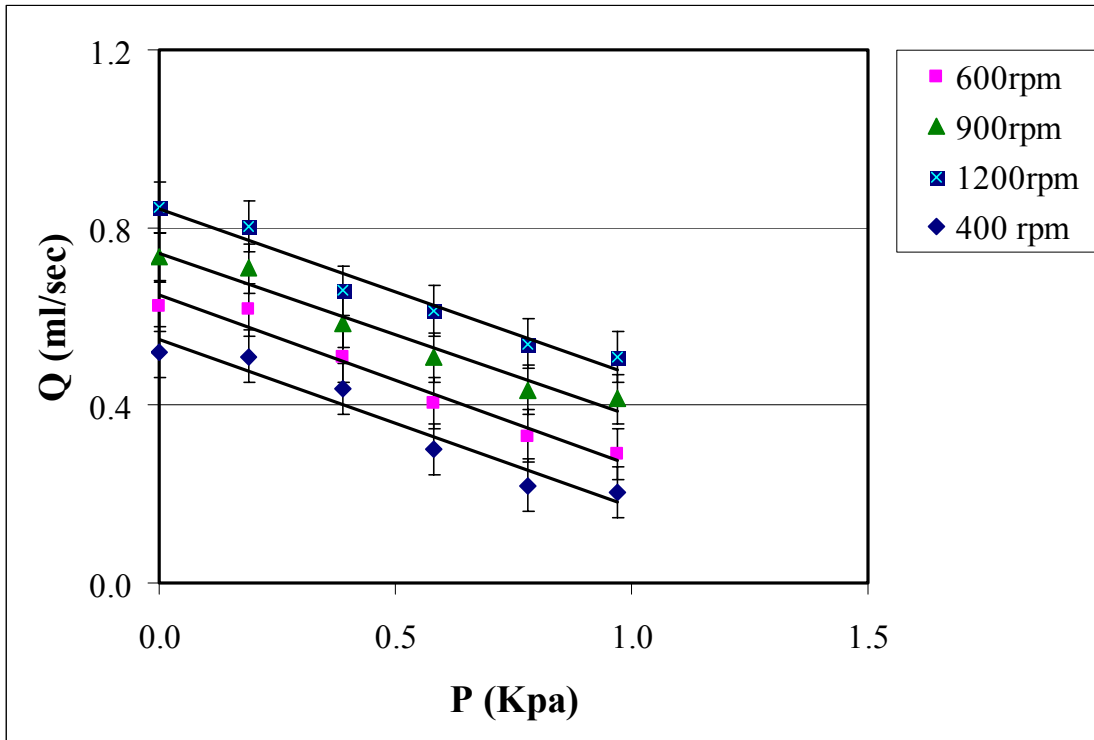


Figure 26: Characteristic plot of a magnetically driven Spiral pump

Table 3: Flow rates summary for mechanically driven meso spiral pump

ΔP (kPa)	Q' at 400 rpm	Q' at 600 rpm	Q' at 900 rpm	Q' at 1200 rpm
0	0.483	0.579	0.678	0.781
0.19	0.476	0.575	0.659	0.746
0.39	0.404	0.472	0.539	0.607
0.58	0.279	0.307	0.472	0.569
0.78	0.156	0.275	0.351	0.498
0.97	0.127	0.181	0.298	0.365

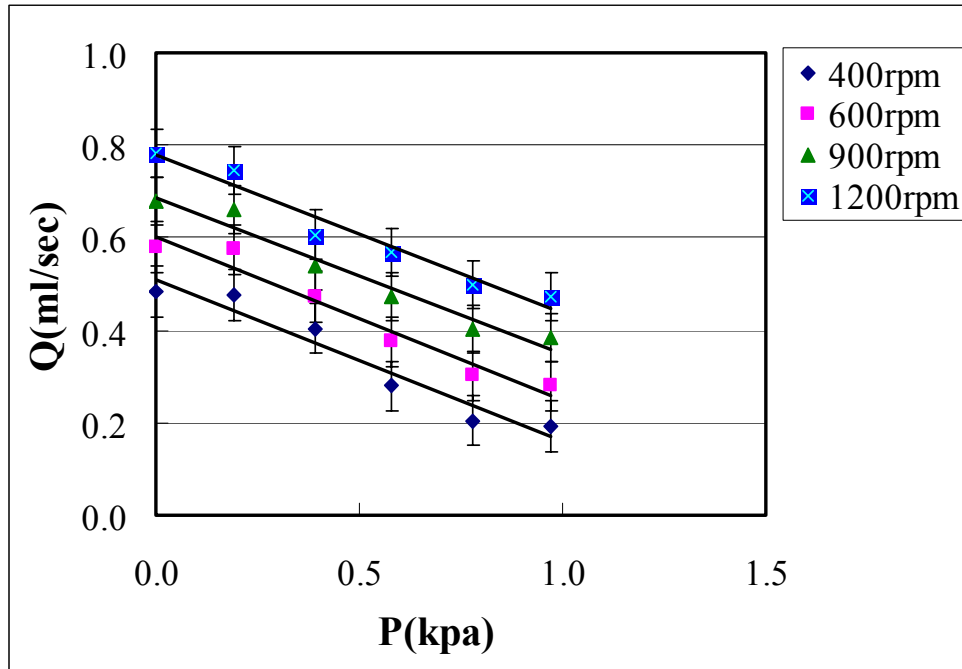


Figure 27: Characteristic plot of a mechanically driven Spiral pump

Figures 26 and 27 display the meso spiral pump characterization when it is magnetically and mechanically driven. Each figure presents four curves describing the mesopump performance when driven at four different speeds. Both figures show that as the pressure head imposed at the outlet tube increases the generated fluid flow decreases. The percentage difference of flow rate between the two mesopumps is approximately 4.2%. The only difference between the two experimentations is that the pump was magnetically and then mechanically driven. The meso spiral pump is used, and motor is powered up by the same power supply.

The analytical equation introduced in chapter one formulating the flow rate of the spiral micropump is

$$Q = \frac{whr}{2} * \omega - \frac{wh^3}{12\mu r(\Delta\theta)} * \Delta P [2]$$

However, because h/w ratio is 0.86, the correction factors F_D , and F_P are added to the previous equation.

$$Q = \left(\frac{whr_a}{2} \omega \right) F_D - \left(\frac{wh^3}{12\mu r_a \Delta\theta} \Delta P \right) F_P \quad [1] \quad (F_D = 0.57, F_P = 0.5)$$

This equation predicts the volumetric performance of the system. By substituting the appropriate constants for the tested spiral and varying the head pressure and rotational speed of the spiral disk, a comparison can be made between experimental and analytical data. Table 4 summarizes the analytical data.

Table 4: Flow rates summary for analytical results of meso spiral pump

ΔP (kPa)	Q at 400 rpm	Q at 600 rpm	Q at 900 rpm	Q at 1200 rpm
0	0.46	0.691	0.679	0.697
0.19	0.42	0.654	0.589	0.604
0.39	0.386	0.616	0.499	0.511
0.58	0.35	0.58	0.409	0.419
0.78	0.312	0.542	0.319	0.326
0.97	0.276	0.506	0.229	0.234

3.1.2 Simulated data of meso spiral pump

The meso spiral pump was simulated and numerical results were summarized in Table 5. Then these simulation results are graphically illustrated in Figure 28.

Table 5: Summary of simulated out flow in (ml/sec) of meso spiral pump

ΔP (kPa)	Q at 400 rpm	Q at 600 rpm	Q at 900 rpm	Q at 1200 rpm
0	0.608	0.72	0.85	0.988
0.19	0.518	0.63	0.76	0.895
0.39	0.428	0.54	0.67	0.802
0.58	0.338	0.45	0.58	0.71
0.78	0.248	0.36	0.49	0.617
0.97	0.160	0.28	0.40	0.525

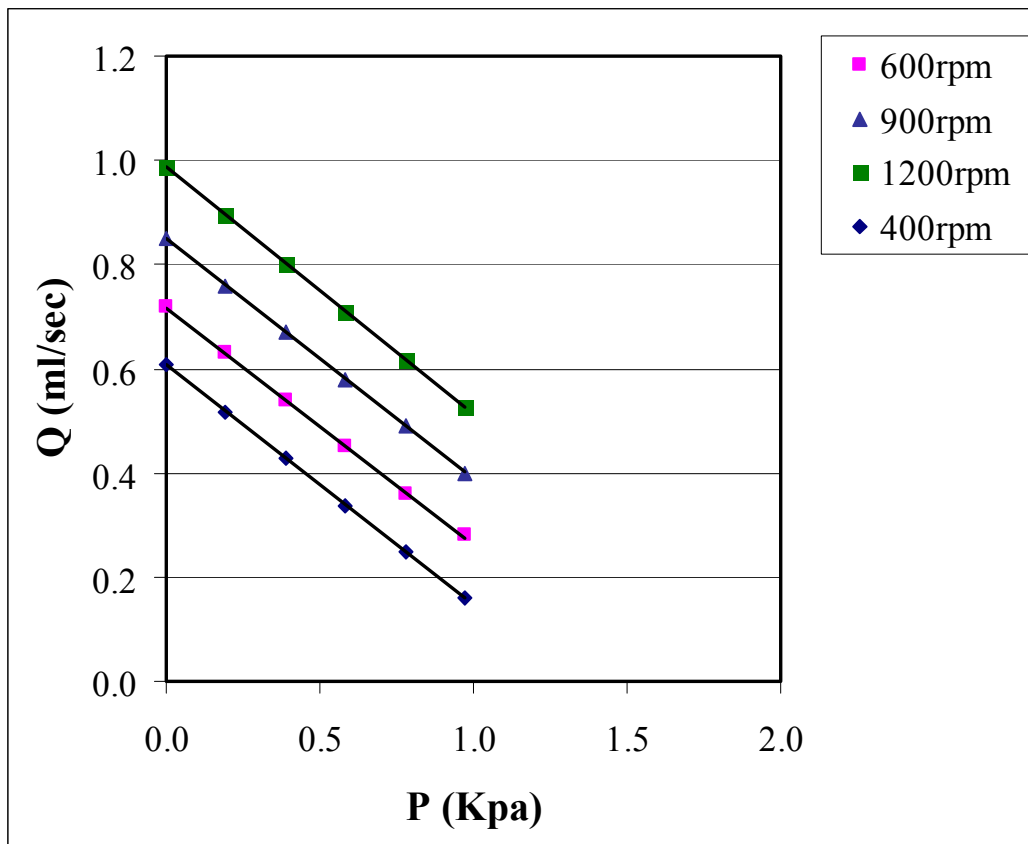


Figure 28: Simulated data characterization at four speeds

In order to analyze and discuss the experimental, analytical, and numerical data at the four speeds, four graphs are plotted, as illustrated in Figures 29, 30, 31, and 32, each comparing the different types of data at particular speed. The characterization curves on each figure are then used to predict the spiral mesopump performance.

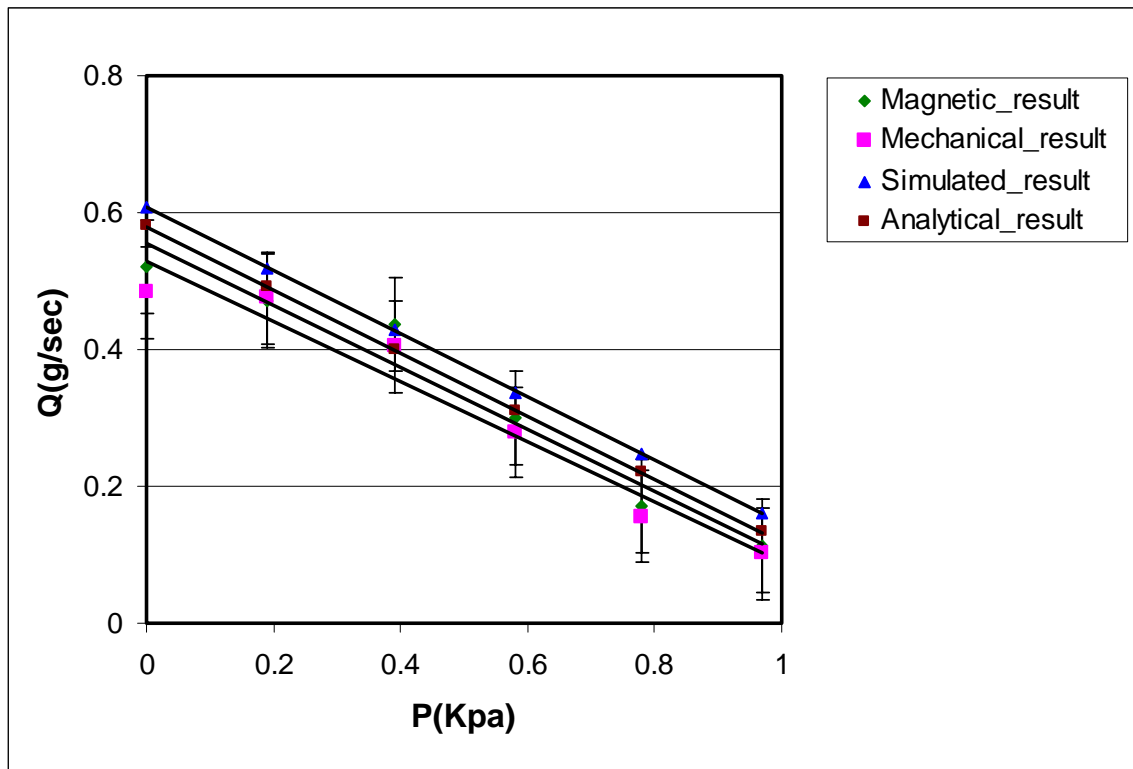


Figure 29: Spiral pump experimental, analytical, and simulated data at 400 rpm

Figures 29, 30, 31, and 32 present the experimental, analytical, and numerical data at four different rotational speeds with the error bars. We notice in these graphs that as the pump speed increases the simulation curve is spreading apart from the experimental curves due to the friction effect in the pump, which is a function of speed. That is, as the speed increases so does the frictional losses. More illustration will be provided later in a subsection describing the viscous drag meso pumps performance.

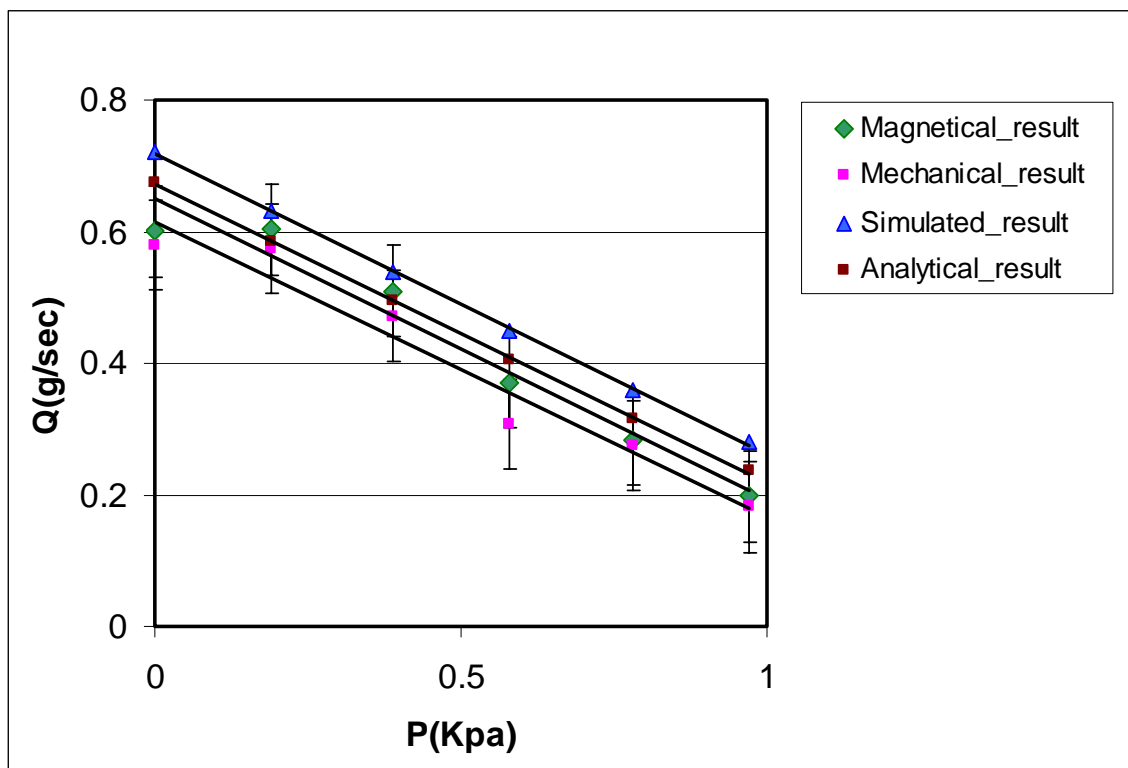


Figure 30: Spiral pump experimental, analytical and simulated data at 600 rpm

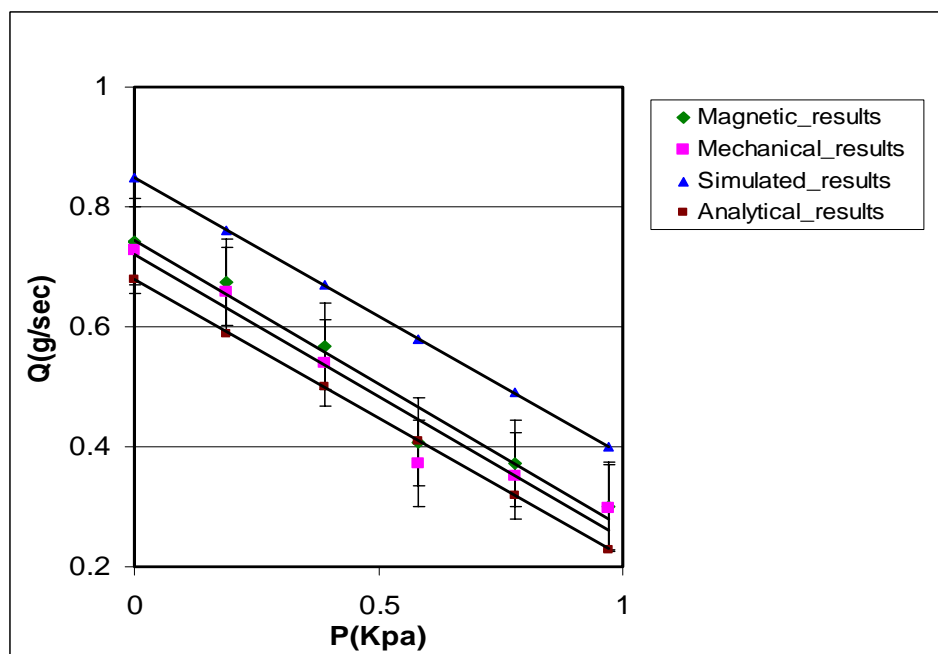


Figure 31: Spiral pump experimental, analytical, and simulated data at 900 rpm

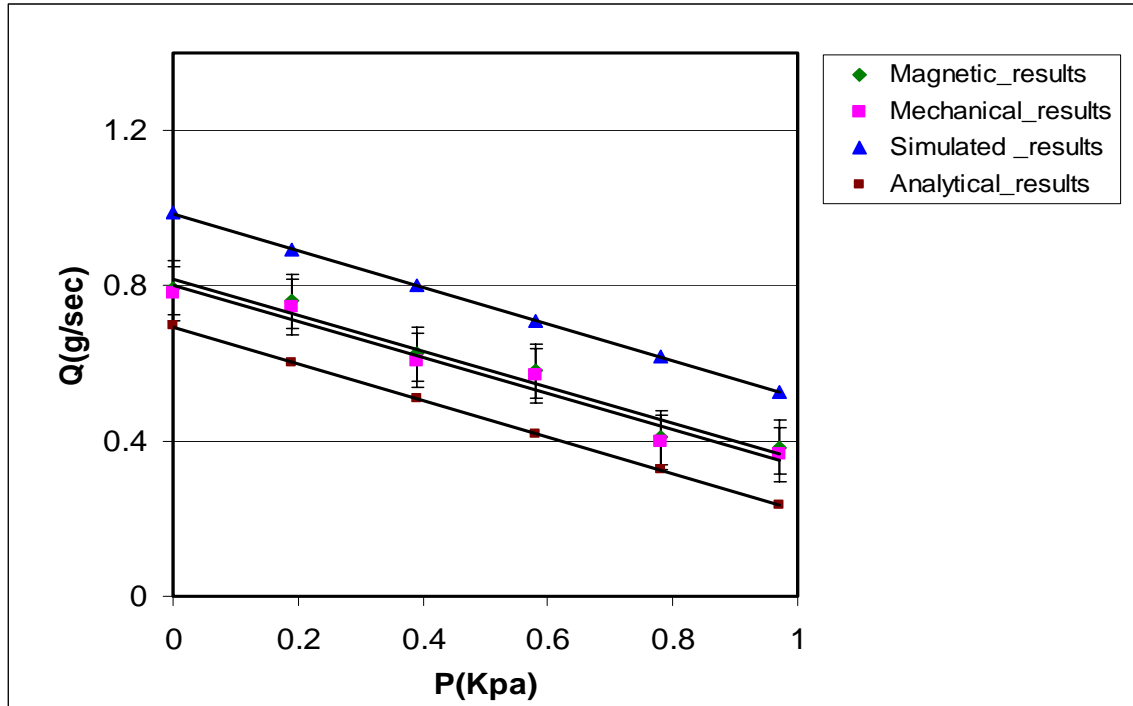


Figure 32: Spiral pump experimental, analytical, and simulated data at 1200 rpm

The figures also show that the experimental flow rates are generally in close agreement with those predicted by analytical solution. At low speeds, the experimental flow rate is slightly below that predicted by analytical solution. This decrease in flow rate may be attributed to the cross flow that will be discussed later in the chapter, the effect of this gap flow is not accounted for in the formula used. It is also observed that when the speed of the pump increases, the experimental flow rate also increases, exceeding that predicted by the analytical solution since the centrifugal effects compensate for the loss in flow rate due to cross flow.

This section presented the gathered experimental, numerical, and analytical results and then transformed those results to data points that were displayed in graphs. The next section will give the generated numerical data, and experimental results for the Von Karman meso pump. The performance curves will then be plotted in graphs to allow us to comment and discuss the viscous drag meso pump's performance.

3.1.3 Results of magnetically and mechanically driven meso Von Karman pumps

Tables 6 summarizes the generated flow rate results when the meso Von Karman pump is magnetically driven at four different rotational speeds, while Table 7 summarizes the generated flow rate results when the meso Von Karman pump is mechanically driven at four different rotational speeds. These flow rates are presented as data points in Figures 33 and 34 where the X-axis is the pressure head (P in kPa), and the Y-axis is the flow rate (Q in ml/sec).

Table 6: Flow rates summary for magnetically driven meso (V/K) pump

ΔP Kpa	Q at 400 rpm	Q at 600rpm	Q at 900 rpm	Q at 1200rpm
0	0.671	0.751	0.834	0.883
0.19	0.642	0.677	0.721	0.812
0.39	0.513	0.626	0.67	0.726
0.58	0.489	0.534	0.578	0.622
0.78	0.324	0.437	0.445	0.519
0.97	0.144	0.196	0.31	0.413

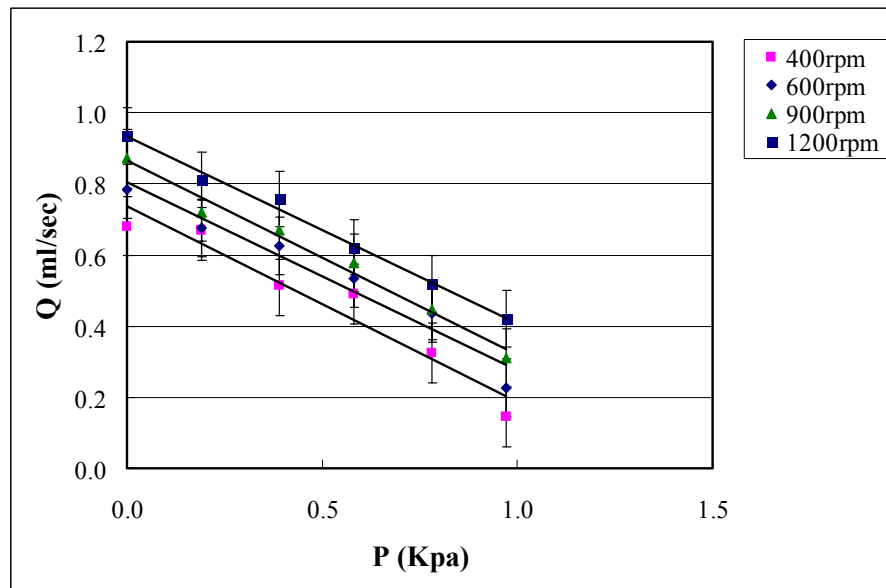


Figure 33: Characteristic plot of a magnetically driven Von Karman pump

Table 7: Flow rates summary for mechanically driven meso (V/K) pump

ΔP Kpa	Q'' at 400 rpm	Q'' at 600rpm	Q'' at 900 rpm	Q'' at 1200rpm
0	0.634	0.730	0.810	0.869
0.19	0.625	0.635	0.674	0.759
0.39	0.476	0.582	0.621	0.702
0.58	0.458	0.500	0.541	0.581
0.78	0.301	0.407	0.413	0.482
0.97	0.135	0.184	0.291	0.394

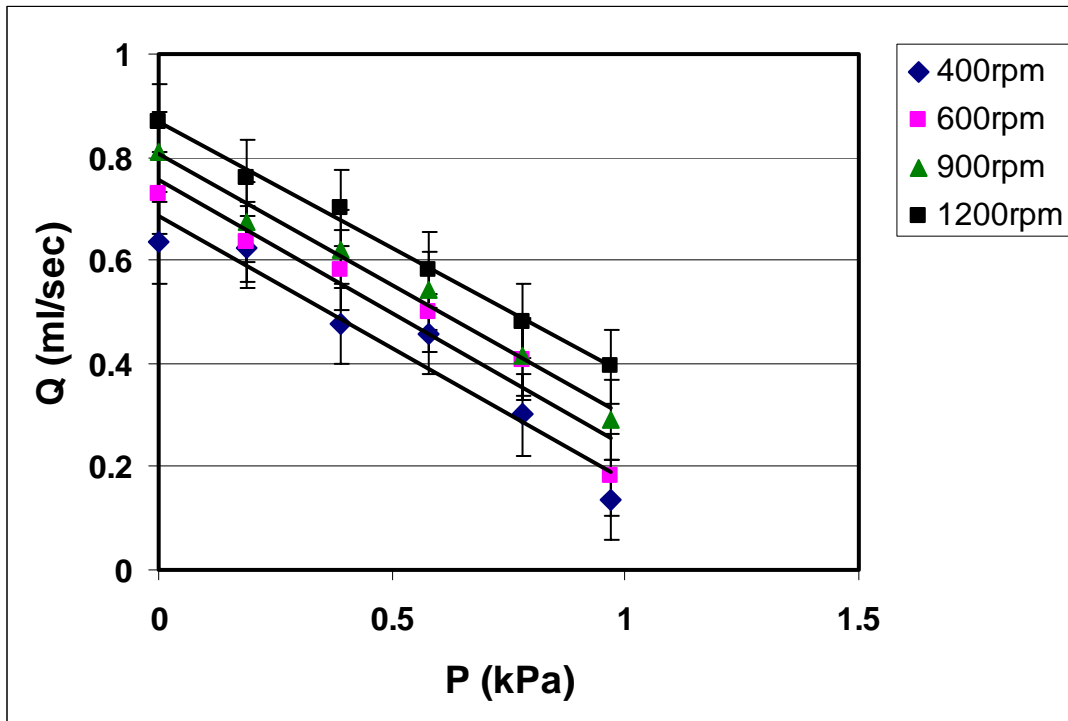


Figure 34: Characteristic plot of a mechanically driven Von Karman pump

Meso Von Karman pump is characterized experimentally for both the magnetically and mechanically driven. Figures 33 and 34 present the pumps performance. Each figure shows four curves describing the mesopump's performance when driven at four different speeds. The percentage difference of flow rate between the magnetically driven and the mechanically driven mesopumps is approximately 4.2%. The reason for this percentage difference is the uncertainty in volume measurements of liquid water due to the graduated cylinder which rounds off more digits. Moreover it is observed that the mesopumps performance curves are following the same trend and therefore the results are close and agreeable.

3.1.4 Simulated data of meso Von Karman pump

Table 8 summarizes the numerical flow rate results when the Von Karman mesopump is simulated. Simulation is performed at different combinations of pressure head and speed. A graph of the pump performance is plotted in Figure 35 showing four characterization curves for simulating the pump at four different speeds. Then an attempt was made to gather the simulated and experimental results in one graph and this was repeated for four different speeds as shown in Figures 36, 37, 38, and 39.

Table 8: Summary of simulated out flow in (ml/sec) for Von Karman mesopump

ΔP kPa	Q at 400 rpm	Q at 600rpm	Q at 900 rpm	Q at 1200rpm
0	0.781	0.883	0.94	1.033
0.19	0.681	0.783	0.84	0.935
0.39	0.583	0.685	0.742	0.837
0.58	0.485	0.587	0.644	0.739
0.78	0.386	0.488	0.545	0.64
0.97	0.286	0.388	0.445	0.54

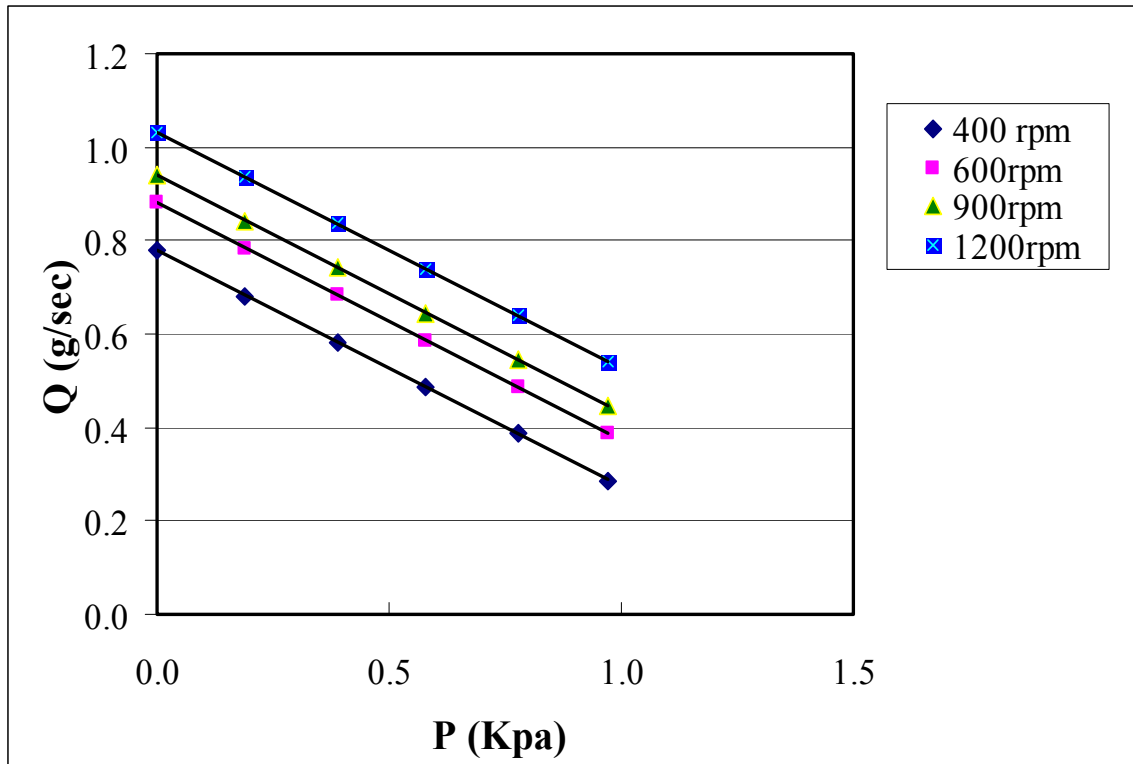


Figure 35: Simulated characterization for meso Von Karman pump

In Figures 36 to 39, the experimental and simulated results are represented as data points, and the characteristic curves are drawn. In each graph, two of the characteristic curves illustrate the Von Karman meso pump performance when it is magnetically and mechanically driven, respectively. The third characteristic curve illustrates the generated simulated results. These plots show the Von Karman pump performance curves when it is tested at four different rotational speeds (400, 600, 900, and 1200) rpm. The analysis of the results, in terms of the performance of the pumps based on the characteristic curves is then done after carefully observing the figures.

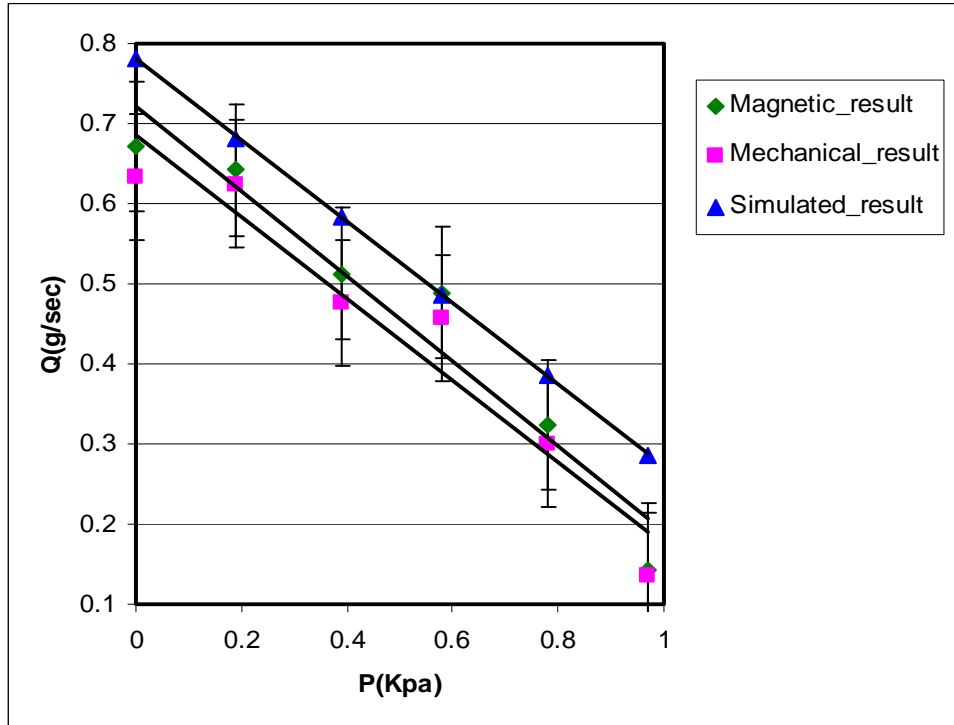


Figure 36: Von Karman experimental and simulated data at 400 rpm

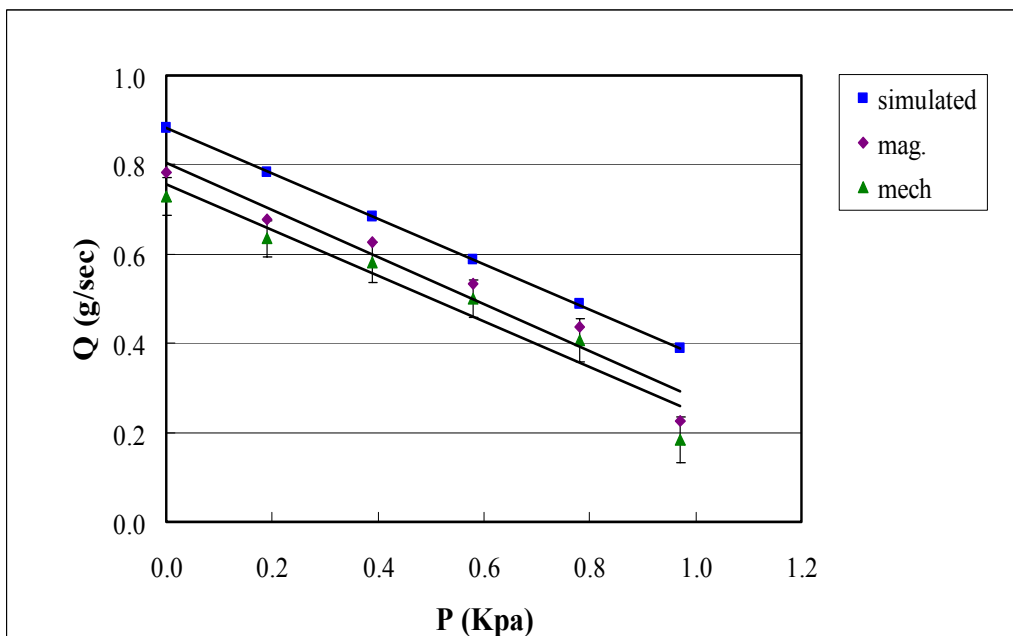


Figure 37: Von Karman experimental and simulated data at 600 rpm

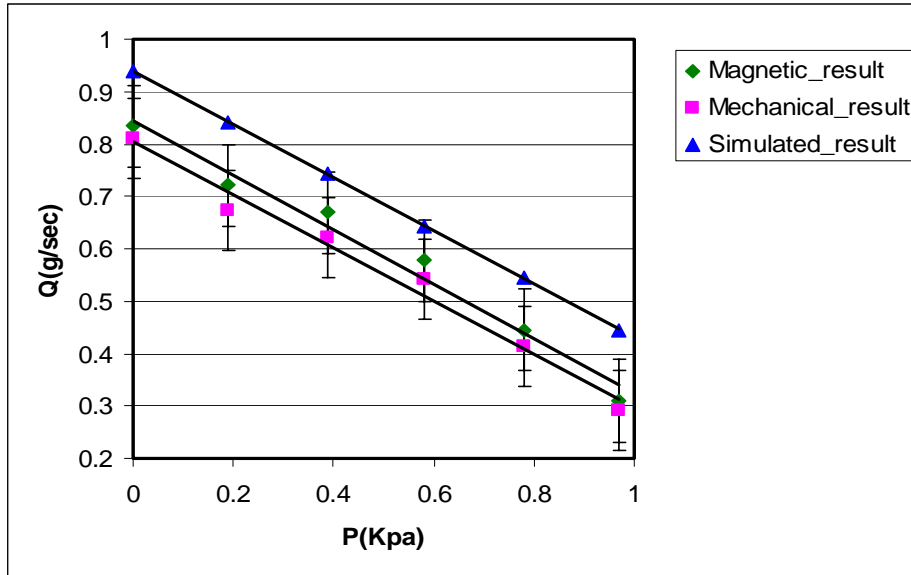


Figure 38: Von Karman experimental and simulated data at 900 rpm

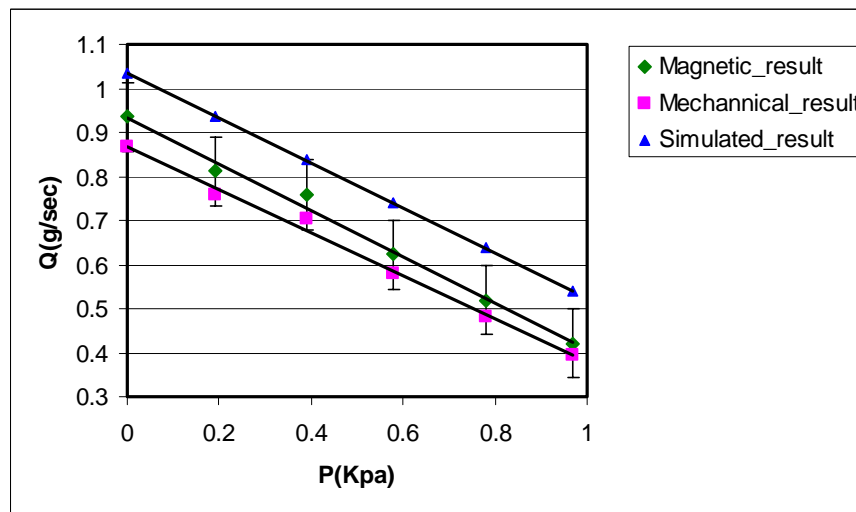


Figure 39: Von Karman experimental and simulated data at 1200 rpm

In Figures 36 to 39, experimental and numerical results are presented at four different rotational speeds. When comparing numerical to simulated data the meso Von Karman results are better than the meso spiral pump results, because as the pump speed increases the simulation curve does not spread apart much from the experimental curves. This performance of meso Von Karman pump is better due to the absence of the spiral channel,

which is the cause of friction in meso spiral pumps. More illustration will be provided later in a subsection describing the viscous drag meso pumps performance.

The previous sections showed the produced results from experimentation and simulation that were presented graphically. The next section will give a description of the viscous drag mesopumps performance including a comparison between experimental and simulated results, and the factors causing the percentage difference between the flow rates values.

3.1.5 Discussion

Magnetic and mechanical results for each meso viscous drag pump (spiral, and Von Karman) are displayed in Figures 26, 27, 33, and 34, which show that the pumped flow rate is linearly decreasing with respect to pressure head and this is due to the created pressure that was built through imposing higher pressure at the outlet than that at the inlet. When the magnetic and mechanical data were gathered in one graph we noticed that the lines are close and parallel for different rpm. Moreover the percentage difference between magnetic and mechanic results for both mesopumps is approximately 4.3 % which is acceptable for the reasons explained before. This implies that both pumps when magnetically and mechanically driven have similar behavior, and the magnetic and mechanical results are in close agreement for each mesopump.

Discussing numerical results for viscous drag pumps, the percentage difference between simulated results and the experimental magnetic results is approximately 19% which is still acceptable. One reason is the gap distance that exists between the top of the spiral wall and the pump house top, which causes a cross flow and the dragging viscous force along the channel to the outlet is reduced, leading to a decrease in flow rate during experimentation. However, as the pump speed increases the centrifugal effect compensates for the loss in flow rate due to cross flow, and the increase in speed would accompany an increase in frictional effect since frictional effect is a function of speed. Moreover, the simulated results presented in Tables 5 and 8 were achieved without taking

into consideration the actual outlet tubing length which is about 52 inches, which when considered would lead to a decrease in flow rate results. For all these reasons the calculated percentage difference is still acceptable. Other factors affecting the percentage difference are packaging and human errors. Finally, since the simulated performance curves of both mesopumps follow the same trend the results are agreeable.

3.2 Positive Displacement Pump Results

3.2.1 Results of magnetically and mechanically driven meso crescent pump

After experimentally running the meso crescent pump, using two driving mechanisms, the flow rate values are gathered in two Tables 9 and 10. The tables presented the flow rate output results of the meso pump when it was magnetically and mechanically driven. The results are graphically presented in Figures 40 and 41. Each figure included four curves describing the meso pump performance at four different rotational speeds.

Table 9: Flow rates summary for magnetically driven meso crescent pump

ΔP kPa	Q at50 rpm	Q at124rpm	Q at131 rpm	Q at140 rpm
0.97	1.354	3.47	3.82	3.98
1.95	1.121	3.42	3.81	3.918
2.93	0.952	3.35	3.723	3.843
3.90	0.918	3.341	3.576	3.822
4.88	0.908	3.196	3.513	3.84
5.86	0.903	3.166	3.486	3.765
6.84	0.897	3.111	3.417	3.604
7.82	0.891	2.948	3.408	3.548
8.79	0.824	2.695	3.263	3.481

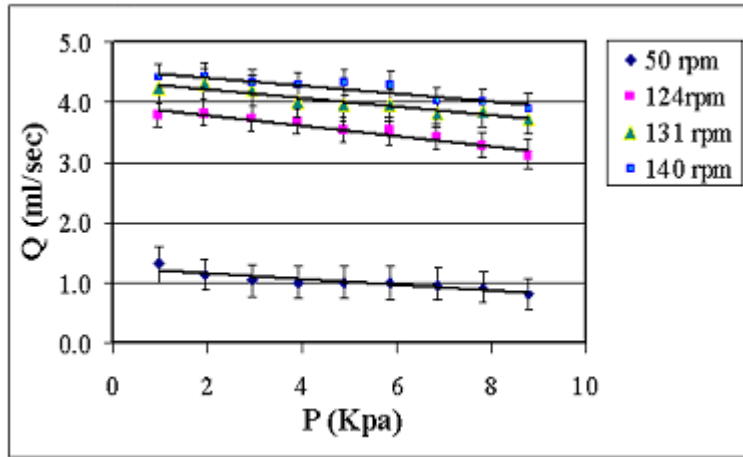


Figure 40: Characteristic plot of a magnetically driven crescent pump

Table 10: Flow rates summary for mechanically driven meso crescent pump

ΔP Kpa	Q at 50 rpm	Q at 124 rpm	Q at 131 rpm	Q at 140 rpm
0.97	1.155	3.306	3.641	3.790
1.95	0.978	3.271	3.622	3.753
2.93	0.914	3.210	3.574	3.689
3.90	0.882	3.214	3.434	3.671
4.88	0.873	3.074	3.375	3.688
5.86	0.868	3.047	3.348	3.618
6.84	0.836	2.995	3.283	3.465
7.82	0.794	2.841	3.278	3.413
8.79	0.697	2.782	3.201	3.353

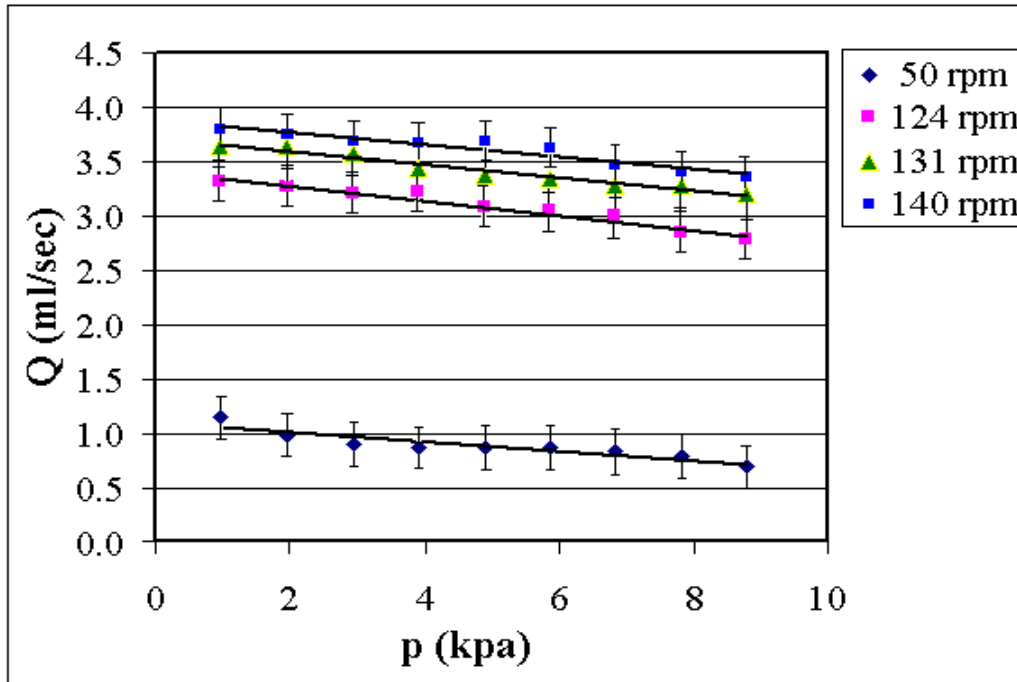


Figure 41: Characteristic plot of a mechanically driven crescent pump

Table 11: Parameters of the crescent pump analytical equation

Parameter (unit)	Values
Height of teeth h (cm)	0.641
Outer radius of the internal gear r_o (cm)	1.56
Inner radius of the internal gear r_i (cm)	0.987
Slit width w (cm)	0.5
Gear diameter d (cm)	2.3
Dynamic Viscosity η (Pa.s)	10^{-3}
Distance between gear and housing h (cm)	0.05
Frequency N (rev/sec)	Set as desired

The analytical equation used to predict the flow rate values of the crescent mesopump is

$$Q = (\pi/2) h (r_o^2 - r_i^2) N - [w (h')^3 / 12 \eta d] \Delta P \quad [1, 5]$$

This equation predicts the volumetric performance of the system. By substituting the appropriate constants in the equation, as defined in Table 11, and varying the head pressure and rotational speed of the pump, a comparison can be made between experimental and analytical data. Table 12 summarizes the analytical flow rate data in (ml/sec) followed by the characteristic curves of the analytical and simulated data.

After substituting the parameters in Table 11, the analytical equation simplifies to the following form.

$$Q = (1.63) N - (0.0022) \Delta P$$

Table 12: Summary of analytical data for the crescent mesopump

ΔP kPa	Q at50 rpm	Q at124rpm	Q at131 rpm	Q at140 rpm
0.97	1.355	3.364	3.555	3.80
1.95	1.353	3.362	3.553	3.798
2.93	1.351	3.360	3.551	3.796
3.90	1.349	3.358	3.549	3.794
4.88	1.347	3.356	3.547	3.792
5.86	1.345	3.354	3.545	3.790
6.84	1.343	3.352	3.543	3.788
7.82	1.340	3.349	3.540	3.785
8.79	1.338	3.347	3.538	3.783

After the experimental and analytical data for the crescent mesopump is collected, it is plotted on a single graph with respect to the pump rotation speed. as shown in Figures 42, 43, 44, and 45. The two mesopumps are operated at four different rotational speeds (50, 124, 131, and 140) rpm, and the three performance curves for the two meso pumps are presented in the same graph for the purpose of drawing a comparison between the generated data and the predicted one.

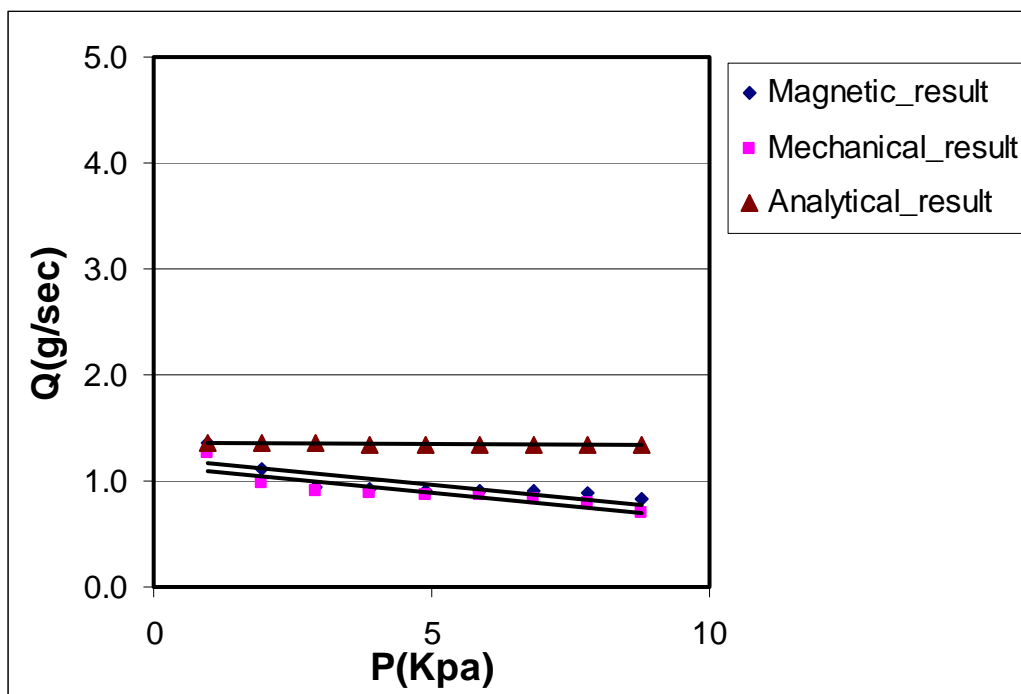


Figure 42: Crescent pump experimental data at 50 rpm

It is noticed in Figures 42 to 45 that the analytical data is approximately a horizontal line and this make sense because the crescent pump is a positive displacement pump which operates through forcing a fixed volume of fluid from the inlet to the outlet. The mesopump provides a fixed displacement per revolution, because the intake is always a constant volume, the flow rate of the discharged fluid is a function of the pump speed only, and the pressure head term in the above equation is insignificant as it is accompanied by its coefficient $[w (h')^3 / 12 \eta d]$ which is 0.0022. Furthermore the

experimental data is agreeable and close to the predicted solution since the slope of the experimental lines is small, hence following the same trend.

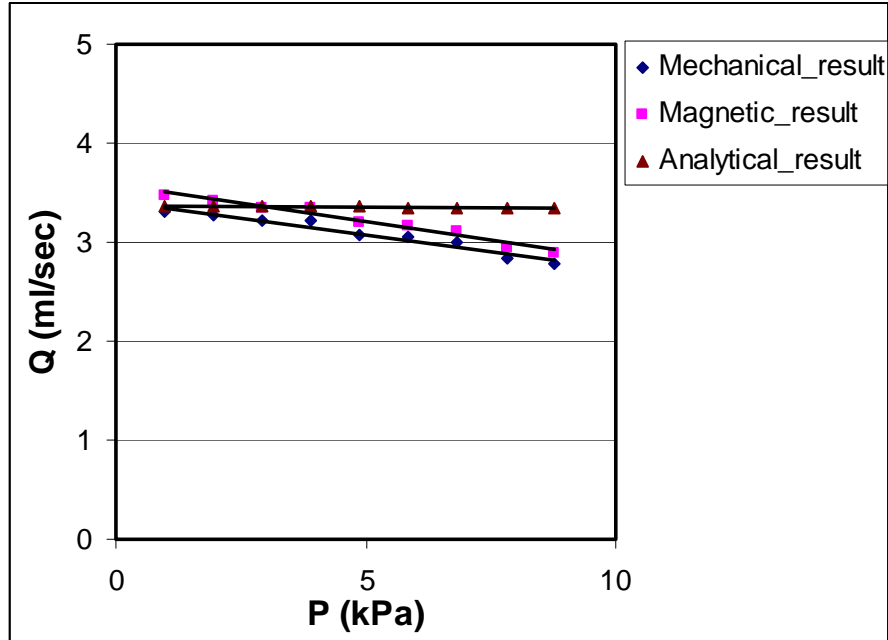


Figure 43: Crescent pump experimental data at 124 rpm

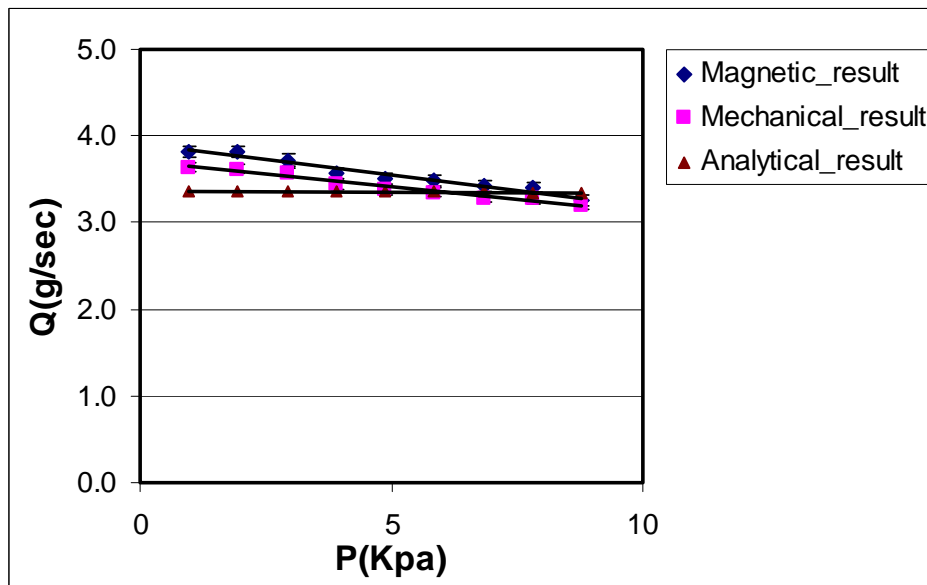


Figure 44: Crescent pump experimental data at 131 rpm

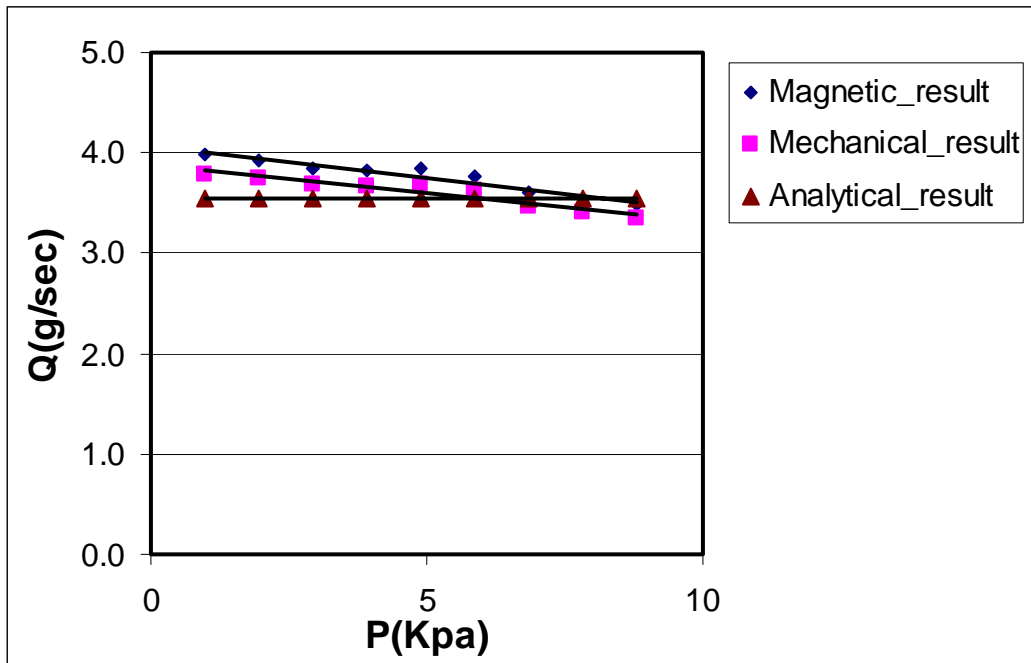


Figure 45: Crescent pump experimental data at 140 rpm

This section described the experimental studies performed to test and characterize the meso crescent pump's performance. To this end, the experimental and analytical data were used to generate characteristic curves of the crescent mesopump performance at different speeds. Those tests provided us with a feedback of the expected generated flow. The next section discusses the generated data.

3.2.2 Discussion

Figures 40 and 41 for the two meso crescent pumps show that the pumped flow rate is linearly decreasing with respect to pressure head but it is a slight decrease where the slope of the line is close to zero. This agrees with the positive displacement principle of crescent pump. Moreover, Figures 42, 43, 44, and 45 shows that the characteristic curves of both mesopumps are close and parallel. The percentage difference between

magnetically driven results and mechanically driven results is approximately 4.1 %; which is an acceptable percentage that shows that experimental results and the performance of both pumps are in close agreement.

CHAPTER 4

CONCLUSIONS & RECOMMENDATIONS

4.1 Conclusions

In order to gain a better understanding of three micropumps (spiral, Von Karman, and crescent) operation, meso scaled pumps were designed, manufactured and experimentally tested. Analytical, computational and Experimental approaches were utilized to achieve a better expected prediction of pump characterization. Each mesopump was magnetically driven and tested, then mechanically driven and tested. Experimental results were obtained and data was gathered in tables, and characterization curves were plotted for each pump as illustrated in chapter three.

Computational simulation was also performed for the spiral and Von Karman mesopumps. Simulated flow rate results were collected and these results were graphically interpreted with their corresponding characteristic curves. Then an analysis of the experimental and simulated data was performed for both spiral and Von Karman mesopumps, followed by a discussion on the analysis. For the crescent mesopump a comparison between experimental results and analytical data was also analyzed and discussed.

Successful testing was performed for the three mesopumps. Experimentation on a magnetically and mechanically driven mesopump produced results that were in close agreement for each pump. The reasons for the increased simulated flow rate results with respect to experimental results were also discussed.

4.2 Recommendations

The primary recommendation for running the micropumps is to get a new amplifier. Currently the present amplifier is not capable of delivering the desired current. Therefore the high current is causing TRA failure, and a circuit was used in lab to produce a quarter of a sine wave signal.

Another recommendation is to design a new generation of micro pumps and to fabricate magnetically driven micro gear system. Since these micro systems will be eventually used for biological purposes, magnetically driven pumps will generate less heat, than mechanically coupled micro pumps, which affects blood tissues and cells. Here lies the importance of using the magnetic coupling technique.

Computational simulation of the crescent pump would also be recommended as a future work. This step would provide us with a prediction of the expected performance of the crescent micropump, and would give us a better understanding of the complex pump flow.

REFERENCES

- 1- Kilani, M., Development of a Surface Micromachined Spiral-Channel Viscous Pump, The Florida State University, 2002
- 2- Hendrix, J, Design & Analysis of Mechanical Micropumps, Florida State University, 2004
- 3- Zheng, P, Magnetic MEMs and its Applications, the Florida State University, 2004
- 4- CFD Research Corporation, Huntsville, Alabama 35805, www.cfdrc.com
- 5- M. Matteucci, F. Perrenes, B. Marmioli, P. Miotti, L. Vaccari, A. Gosparini, A. Turchet, and E. Di Fabrizio; Compact micropumping system based on LIGA fabricated microparts; Microelectronic Engineering; 83 (4); 2006
- 6- Hsu, Tai-Ran, MEMS and MICROSYSTEMS, Design and Manufacture, McGraw Hill, 2002
- 7- MEMS Advanced Design Short Course, Sandia National Laboratories, 2003

BIOGRAPHICAL SKETCH

Omar Al-Rifai was born on December 16, 1976, in Tripoli, Lebanon. He attended elementary school and high school in Tripoli. He then pursued his Bachelors degree in the field of Mechanical engineering in 2001 after completing the requirements of *Beirut University*, in Beirut, Lebanon, he served in the Lebanese military as a Second Lieutenant for one year. After completing his military service, Omar enrolled at FSU to pursue his Masters degree in mechanical engineering, under the supervision of Dr. Yousef Haik, in the field of *fluids*. He defended his thesis during fall 2005 semester and plan to pursue a doctorate degree in the near future.